

A Steep Slope and Small Scatter for the High-Mass End of the L - σ Relation at $z \sim 0.55$

Antonio D. Montero-Dorta^{1*}, Yiping Shu¹, Adam S. Bolton¹, Joel R. Brownstein¹, Benjamin J. Weiner²

¹ *Department of Physics and Astronomy, The University of Utah, 115 South 1400 East, Salt Lake City, UT 84112, USA*

² *Steward Observatory, 933 N. Cherry Ave., University of Arizona, Tucson, AZ 85721, USA*

Accepted —. Received —; in original form —

ABSTRACT

We measure the intrinsic relation between velocity dispersion (σ) and luminosity (L) for massive, luminous red galaxies (LRGs) at redshift $z \sim 0.55$. We achieve unprecedented precision by using a sample of 600,000 galaxies with spectra from the Baryon Oscillation Spectroscopic Survey (BOSS) of the third Sloan Digital Sky Survey (SDSS-III), covering a range of stellar masses $M_* \gtrsim 10^{11} M_\odot$. We deconvolve the effects of photometric errors, limited spectroscopic signal-to-noise ratio, and red–blue galaxy confusion using a novel hierarchical Bayesian formalism that is generally applicable to any combination of photometric and spectroscopic observables. For an L - σ relation of the form $L \propto \sigma^\beta$, we find $\beta = 7.8 \pm 1.1$ for σ corrected to the effective radius, and a very small intrinsic scatter of $s = 0.047 \pm 0.004$ in $\log_{10} \sigma$ at fixed L . No significant redshift evolution is found for these parameters. The evolution of the zero-point within the redshift range considered is consistent with the passive evolution of a galaxy population that formed at redshift $z = 2 - 3$, assuming single stellar populations. An analysis of previously reported results seems to indicate that the passively-evolved high-mass L - σ relation at $z \sim 0.55$ is consistent with the one measured at $z = 0.1$. Our results, in combination with those presented in Montero-Dorta et al. (2014), provide a detailed description of the high-mass end of the red sequence (RS) at $z \sim 0.55$. This characterization, in the light of previous literature, suggest that the high-mass RS distribution corresponds to the “core” elliptical population.

Key words: surveys - galaxies: evolution - galaxies: kinematics and dynamics - galaxies: statistics - methods: analytical - methods: statistical

1 INTRODUCTION

In the 60’s and 70’s, several empirical scaling relations between the kinematic and photometric properties of early-type galaxies (ETGs) were identified. Thanks to the seminal work of Djorgovski & Davis (1987) and Dressler et al. (1987), today we know that these relations are different projections of the so-called *fundamental plane* (FP) of ETGs, which is a thin plane outlined by the occupation of ETGs in the three-dimensional space spanned by velocity dispersion,

effective radius and surface brightness, i.e., $\log_{10} \sigma$, $\log_{10} R_e$, and $\log_{10} \langle I \rangle_e$, respectively.

Of particular interest among these scaling relations is the L - σ relation, a specific two-dimensional projection of the FP that relates the luminosity L and the central stellar velocity dispersion σ of ETGs. This relation was first reported by Minkowski (1962), using a sample of only 13 ETGs, and by Morton & Chevalier (1973) a decade later, although no quantification was provided. The relation was first quantified in a sample of 25 galaxies by Faber & Jackson (1976), as a power law in the form $L \propto \sigma^4$, and has been commonly called the *Faber-Jackson Relation* (F-J relation) since then.

* E-mail: amonero@astro.utah.edu

As a link between a distance-independent quantity σ and an intrinsic property L , the F-J relation immediately became a useful distance estimator and consequently a cosmological probe (e.g., de Vaucouleurs 1982a,b; Paturel & Garnier 1992).

With the emergence of large-scale structure (LSS) galaxy surveys in the last decades, the size of the ETG samples available increased dramatically, especially at low redshift, i.e. $z \sim 0.1$ (mostly with the Sloan Digital Sky Server, SDSS, York et al. 2000). It was then confirmed with statistical significance, that the L - σ relation at intermediate masses/luminosities approximately follows a canonical F-J relation with a slope of ~ 4 (note that the words “slope” and “exponent” are commonly used interchangeably, as the relation is often expressed in the form $M \propto \log_{10} \sigma$, where M is the absolute magnitude). This result is reported in, e.g., Bernardi et al. (2003a) and Desroches et al. (2007), along with a typical scatter in $\log_{10} \sigma$ of ~ 0.1 dex.

Almost since the very discovery of the L - σ relation, however, it became clear that the slope depended on the luminosity range of the sample under analysis. A value of $\gtrsim 4.5$ has been measured in luminous ETGs (e.g., Schechter 1980; Malumuth & Kirshner 1981; Cappellari et al. 2013; Kormendy & Bender 2013) and ~ 2 in faint ETGs (e.g., Tonry 1981; Davies et al. 1983; Held et al. 1992; de Rijcke et al. 2005; Matkovic & Guzmán 2007). A confirmation of the curvature of the L - σ relation towards the high-mass end with high statistical significance has been possible thanks to the SDSS (see Desroches et al. 2007; Hyde & Bernardi 2009a; Nigoche-Netro et al. 2010; Bernardi et al. 2011). The $z \sim 0.1$ sample of Bernardi et al. 2011, as an example, contains $\sim 18,000$ ETGs with $\log_{10} M_* \gtrsim 11.2/11.5$. As the F-J relation, where $L \propto \sigma^4$, is therefore a particular, canonical case that only appears to hold for morphologically selected samples at intermediate mass ranges, in the remainder of this paper we adopt the generic “ L - σ relation” terminology.

The curvature of the L - σ relation is a consequence of the curvature of the FP itself. In fact, the phenomenology of the FP has turned out to be rather complex. Enough evidence has been gathered that its characteristics depend, not only on luminosity/stellar mass but, to a greater or lesser degree, on a variety of other galaxy properties. In addition, the sensitivity of the measurements to selection effects and low-number statistics has often lead to contradictory results. In terms of redshift evolution, it appears clear that the zero-point of the FP must evolve from $z \sim 1$ in a way that approximates that of a passively-evolving galaxy population (e.g., Bernardi et al. 2003b; Jørgensen et al. 2006). However, there are some indications that the FP might be significantly steeper at higher redshifts (Jørgensen et al. 2006; Fritz et al. 2009), whereas for the intrinsic scatter, conclusions are so far somewhat contradictory (e.g., Nigoche-Netro et al. 2011 measure a decrease in the scatter of the the L - σ relation, whereas results from Shu et al. 2012 appear to indicate the opposite). It seems that the

properties of the FP also depend, to some extent, on the wavelength range probed, which is an indication that stellar population properties have an impact on the FP. While these properties appear to remain fairly unchanged in the optical (Bernardi et al. 2003b; Hyde & Bernardi 2009b), there are clear indications that the FP is intrinsically different in the infrared (e.g., Pahre et al. 1998; La Barbera et al. 2010; Magoulas et al. 2012). The dependence of the FP on environment has also been the subject of a number of works (see e.g. Treu et al. 2001; Bernardi et al. 2003b; Reda et al. 2004, 2005; Denicoló et al. 2005; La Barbera et al. 2010, for the FP; Focardi & Malavasi 2012 for the L - σ relation). This is not by any means a complete list; a number of other galaxy properties have been investigated in recent years.

While the use of the FP and its projections as a cosmological probe has been largely eclipsed by other techniques, the FP has gained increasing attention in the last decades as a source of observational constraints for galaxy formation and evolution theories. In this sense, the variation and evolution trends with respect to galaxy properties in the slope and intrinsic scatter of the FP and its projections are believed to be the imprints of non-homological physical processes that occur during the formation and evolution of galaxies. Understanding these observed trends provides crucial insight into these fundamental processes. In this sense, recent cosmological simulations have investigated the impacts of various physical processes such as major/minor mergers and disc instabilities on shaping the internal structure and kinematic properties of ETGs (e.g., Oser et al. 2012; Shankar et al. 2013; Posti et al. 2014; Porter et al. 2014).

In this paper, we use data from the Baryon Oscillation Spectroscopic Survey (BOSS, Dawson et al. 2013) of the SDSS-III (Eisenstein et al. 2011) to measure, for the first time, the high-mass end of the L - σ relation at $0.5 < z < 0.7$. This is a continuation of the work presented in Montero-Dorta et al. (2014), hereafter MD2014, where the intrinsic colour-colour-magnitude red sequence (RS) distribution is deconvolved from photometric errors and selection effects in order to compute the evolution of the RS luminosity function (LF). An important conclusion of MD2014 is that, at fixed apparent magnitude, and for a narrow redshift slice, the RS is an extremely narrow distribution (< 0.05 mag), consistent with a single point in the optical colour-colour plane. This work is intended to measure the L - σ relation that this photometrically distinct population obeys. At intermediate redshifts, the BOSS capability to characterize the massive RS population is unrivaled, with a huge sample of more than 1 million luminous red galaxies (LRGs) with stellar masses $M_* \gtrsim 10^{11} M_\odot$. No other previous survey or sample has been able to probe this population with comparable statistics, hence the unique value of the measurements reported here (find a preliminary analysis from BOSS in Shu et al. 2012, where incompleteness is, however, only partially addressed). Importantly, our intrinsic RS was identified in MD2014 using exclusively photometric information, i.e. our red-blue deconvolution is based on the phenomenol-

ogy of the colour-colour plane, and not on any morphological classification. We will, therefore, use the “RS” terminology instead of the “ETG” terminology when referring to our sample/results.

The mass range covered by BOSS has been hard to probe at $z \sim 0.55$. In fact, most of the information that we have about the high-mass end of the L - σ relation comes from the SDSS at $z \sim 0.1$ or from small samples of very-nearby ETGs, using high-resolution observations (the latter being strongly affected by low-number statistics and selection effects). One of the most important discoveries from these studies is that the slope of the L - σ relation is steeper at higher masses/luminosities, as mentioned above. In recent years, a picture that attempts to explain this mass dependence has emerged. The curvature in the scaling relations has been associated with a characteristic stellar mass scale of $\sim 2 \times 10^{11} M_{\odot}$. This scale, which was first reported at high significance by Bernardi et al. (2011) with the SDSS, is thought to be related to a change in the assembly history of galaxies (recently, Bernardi et al. 2014 have shown that this scale is also special for the late-type galaxy population).

High-resolution imaging has shown that the high-mass scale marks the separation between two distinct ETG populations: *core ellipticals* are defined by the fact that the central light profile is a shallow power law separated by a break from the outer, steep Sersic function profile, whereas in *coreless ellipticals* (also known as “power-law” or “cusp” ellipticals) this feature is not present (see e.g. Lauer et al. 2007b,a). It has been shown in small samples that core ellipticals dominate at the high-mass end, while coreless ellipticals are predominant at lower masses (Kormendy & Bender 1996; Faber et al. 1997; Hyde et al. 2008; Cappellari et al. 2013; Kormendy & Bender 2013). Importantly, this bimodality in the central surface brightness profile extends to a variety of other properties. The distinct characteristics of each of these types, including the fact that core ellipticals obey an L - σ relation with a significantly steeper slope (Lauer et al. 2007b; Kormendy & Bender 2013), have been associated with 2 different evolutionary paths for these objects. Core ellipticals are thought to be formed through major dissipationless mergers (Desroches et al. 2007; von der Linden et al. 2007; Hyde et al. 2008; Lauer et al. 2007a; Bernardi et al. 2011; Cappellari et al. 2013; Kormendy & Bender 2013), whereas coreless ellipticals might have undergone more recent episodes of star formation (Kormendy et al. 2009 review evidence that they are formed in wet mergers with starbursts).

To complement the work done in MD2014, here we present a novel method to combine photometric and spectroscopic quantities in low signal-to-noise (SN) large-photometric-error samples that we call *Photometric Deconvolution of Spectroscopic Observables* (hereafter, PDSO). The PDSO is a hierarchical Bayesian statistical method that allows us to combine the velocity dispersion likelihood function measurements of Shu et al. (2012) with the photometric

red/blue deconvolution of MD2014 to provide the most precise measurement ever performed of the high-mass end of the intrinsic L - σ relation within the redshift range $0.5 < z < 0.7$.

This paper is organized as follows. Section provides an overview of methods and motivations. In Section 3 we briefly describe the target selection for the galaxy sample that we use, the BOSS CMASS sample (3.1), and the computation of stellar velocity dispersion likelihood functions from Shu et al. (2012) (3.2). Section 4 is devoted to summarizing the results of MD2014 regarding the intrinsic RS colour-colour-magnitude distribution. In Section 5, we present our PDSO method in a general form (5.1) and we address the application of our method to the BOSS CMASS sample (5.2). In Section 6, we describe our aperture correction procedure. In Section 7 we present the best-fit parameters for the σ – apparent magnitude relation (7.1), discuss the effect of addressing completeness and the red/blue population deconvolution (7.2) and present our the L - σ relation results (7.3). In Section 8, we compare our measurements with previous results from the literature (8.1) and discuss on the physical implications of our measurements (8.2). Finally, we summarize our main conclusions and discuss future applications in Section 9. Throughout this paper we adopt a cosmology with $\Omega_M = 0.274$, $\Omega_{\Lambda} = 0.726$ and $H_0 = 100h$ km s $^{-1}$ Mpc $^{-1}$ with $h = 0.70$ (WMAP7, Komatsu et al. 2011), and use AB magnitudes (Oke & Gunn 1983).

2 OVERVIEW OF METHODS AND MOTIVATIONS

The statistical power of BOSS to cover the very-massive RS population is unrivaled at $z \sim 0.55$, with a sample of ~ 1 million galaxies (in the latest data release, see Alam et al. 2015) with stellar masses $M_{*} \gtrsim 10^{11} M_{\odot}$ and a median stellar mass of $M_{*} \simeq 10^{11.3} M_{\odot}$ (as measured by Maraston et al. 2013, assuming a Kroupa (2001) initial mass function). The samples, however, present significant challenges, including low SN ratio for the spectra, large photometric errors and a selection scheme that allows for a fraction of bluer objects that increases with redshift. The photometric issues are addressed in MD2014, where we photometrically deconvolve the intrinsic red sequence distribution from photometric errors and selection effects. Our red–blue population deconvolution allows us to characterize completeness in the CMASS sample, which is the main LRG sample from BOSS, covering a redshift range $0.4 < z < 0.7$ (see next section for a complete description of the sample). This characterization allows us to analyze the luminosity function and colour evolution of the LRG population.

The aforementioned analysis in MD2014 is performed within the framework of a Bayesian hierarchical statistical method that is aimed at constraining distributions of galaxy properties, instead of individual-galaxy properties (since an object-by-object approach is discouraged by the characteristics of the BOSS data). The same philosophy is applied in

this work to compute the high-mass end of the L - σ relation. The main steps of our analysis are:

- Development of a general Bayesian hierarchical statistical method that combines the photometric red-blue deconvolution and selection function from MD2014 with probability density information from a spectroscopic observable. We call this formalism *photometric deconvolution of spectroscopic observables* or PDSO. Our method is aimed at constraining the hyper-parameters of a model for the joint pdf of survey galaxies in physical parameter space, by marginalizing over the physical parameter likelihood functions of individual galaxies given the survey data.
- Application of the above formalism to the computation of the best-fit intrinsic L - σ relation from BOSS. The idea is to parametrize the intrinsic distribution in L - σ space, and use the PDSO method to constrain the parameters of this distribution: the slope, zero-point and the intrinsic scatter of the L - σ relation.
- Evaluation of the redshift evolution of the best-fit parameters that define the L - σ relation within a suitable redshift range, namely $0.5 < z < 0.7$.

The results of the above analysis will add important constraints to the evolution of massive RS galaxies. In addition, the PDSO method will lay the foundations for future BOSS studies, where the intrinsic distributions of spectroscopically-derived quantities can be determined. In the broader picture, an important goal of this paper is to complement the detailed characterization of the main statistical properties of the LRG population initiated in MD2014 that will be eventually used, in combination with N-body numerical simulations, to investigate the intrinsic clustering properties of these systems and the halo-galaxy connection in a fully consistent way. The connection between galaxies and halos will be performed by applying the techniques of halo occupation distributions (HOD: e.g., Berlind & Weinberg 2002; Zehavi et al. 2005) and halo abundance matching (HAM: e.g., Vale & Ostriker 2004; Trujillo-Gomez et al. 2011). These future applications are addressed in more detail in the last section of the paper.

3 THE DATA

3.1 The CMASS sample

In this work we make use of both spectroscopic and photometric data from the Tenth Data Release of the SDSS (DR10, Ahn et al. 2014), which corresponds to the third data release of the SDSS-III program and the second release that includes BOSS data. We choose the DR10 instead of the recently published Data Release 12 (DR12, Alam et al. 2015), in order to be consistent with the luminosity function results shown in MD2014. The spectroscopic DR10 BOSS sample contains a total of 927,844 galaxy spectra and 535,995 quasar spectra (this is a growth of almost a factor two as compared to the SDSS DR9, Ahn et al.

2012). The baseline imaging sample is the final SDSS imaging data set, which contains, not only the new SDSS-III imaging, but also the previous SDSS-I and II imaging data. This imaging data set was released as part of the DR8 (Aihara et al. 2011). These imaging programs provide five-band *ugriz* imaging over 7600 sq deg in the Northern Galactic Hemisphere and ~ 3100 sq deg in the Southern Galactic Hemisphere. The typical magnitude corresponding to the 50% completeness limit for detection of point sources is $r = 22.5$. The following papers provide comprehensive information about technical aspects of the SDSS survey: Fukugita et al. (1996) describes the SDSS *ugriz* photometric system; Gunn et al. (1998) and Gunn et al. (2006) describe the SDSS camera and the SDSS telescope, respectively; Smee et al. (2013) provides detailed information about the SDSS/BOSS spectrographs.

The catalog that we used to compute the RS LF in MD2014 is the DR10 Large Scale Structure catalog (DR10 LSS). The DR10 LSS, which is basically built from the BOSS spectroscopic catalog and is thoroughly described in Anderson et al. (2014), contains a small number of galaxies from the SDSS Legacy Survey. The SDSS Legacy Survey includes the SDSS-I survey and a small fraction of the SDSS-II survey. In the previous SDSS programs, the spectra were observed through 3 arcsec fibers, while the aperture size is only 2 arcsec for BOSS. This varying aperture size makes the LSS catalog slightly heterogeneous as far as the velocity-dispersion measurement is concerned. To avoid this problem, we opt to use the spectroscopic catalog, which is very similar to the LSS catalog, and essentially maps the same intrinsic population as that described by the RS LF presented in MD2014. We have also checked that SDSS Legacy galaxies are confined to a very small region of low redshift and high luminosity within the redshift-luminosity space. Importantly, they are mostly found at $z \lesssim 0.5$, which is below the redshift range where our LF results are reliable ($0.52 \lesssim z \lesssim 0.65$, see MD2014).

We restrict our analysis to the CMASS (for ‘‘Constant MASS’’) spectroscopic sample of the BOSS spectroscopic catalog. This sample is built within the official SDSS-III pipeline by first applying an imaging pre-selection to ensure that only detections passing a particular set of quality criteria are chosen as targets. Secondly, a set of colour-magnitude cuts is applied to the resulting catalog, intended to select the LRG sample required to effectively measure the BAO within a nominal redshift range $0.43 < z < 0.70$ (the sample extends slightly beyond these limits). In a similar way, the low-redshift LOWZ sample (not used in this paper) is constructed, covering a nominal redshift range $0.15 < z < 0.43$. For more information on the BOSS selection refer to Eisenstein et al. (2011), Dawson et al. (2013) and Reid et al. (2015) (also a summary is provided in MD2014). Importantly, the CMASS selection allows for a fraction of $\sim 37\%$ of blue cloud objects, as measured by MD2014. The stellar masses for the red population, as measured by Maraston et al. (2013), are $M_* \gtrsim 10^{11} M_\odot$, peaking

at $M_* \simeq 10^{11.3} M_\odot$, assuming a Kroupa initial stellar mass function (Kroupa 2001). All colours quoted in this paper are *model* colours and all magnitudes *cmodel* magnitudes.

The total number of unique CMASS galaxies with a good redshift estimate and with model and cmodel apparent magnitudes and photometric errors in all g,r and i bands in the catalog is 549,005. The mean redshift in the sample is 0.532 and the standard deviation 0.128; approximately $\sim 7.5\%$ and $\sim 4.5\%$ of galaxies lie below and above the nominal low redshift and high redshift limits, i.e., $z = 0.43$ and $z = 0.70$, respectively. For a complete discussion on the selection effects affecting the CMASS data, see MD2014.

3.2 Velocity dispersion likelihood functions

One of the key ingredients in our L - σ relation study is the likelihood function of the central stellar velocity dispersion. The method for determining this likelihood function is described in detail in Shu et al. (2012). Here we provide a brief summary. For every galaxy in our sample, the line-of-sight stellar velocity dispersion within the central circular region of radius 1 arcsec, is measured spectroscopically by fitting a linear combination of broadened stellar *eigenspectra* to the observed galaxy spectrum (note that the typical seeing for BOSS is 1.5 arcsec). Thus, for the i^{th} galaxy, the χ^2 of the fit as a function of the trial velocity dispersion is converted into the likelihood function of velocity dispersion with respect to the observational data d_i as

$$p(d_i | \log_{10} \sigma) \propto \exp[-\chi_i^2(\log_{10} \sigma)/2]. \quad (1)$$

The best-fit velocity dispersion and its uncertainty can then be inferred from the χ^2 function.

Figure 1 illustrates the type of velocity dispersion data that we have in BOSS. In the bottom panel, the best-fit central velocity dispersion and its uncertainty are shown in a scatter plot for all red CMASS galaxies within the redshift slice $z = 0.55 \pm 0.005$. Here, a simple colour cut $g - i > 2.35$ is used to approximately remove blue galaxies in observed space (following Masters et al. 2011). This is just illustrative, as in MD2014 we demonstrate that a simple colour cut is not efficient in terms of isolating the intrinsic RS, as large photometric errors scatter objects in and out of the colour demarcation. At $z = 0.55$ the colour cut removes 20% of the sample. The fraction of intrinsically non-RS objects in the CMASS sample at the same redshift according to the population deconvolution of MD2014 is 38%.

The two quantities shown in Figure 1 are inferred from the velocity-dispersion likelihood functions. Figure 1 shows that the distribution is centered around $\log_{10} \sigma \simeq 2.35$, or 220 km/s, and $\Delta \log_{10} \sigma \simeq 0.06$ dex, or 30 km/s. More than two-thirds of the subsample have velocity dispersions between 120 km/s and 300 km/s with 20 – 50 km/s uncertainties. The top panel displays an example of a typical χ^2 function of a galaxy with both velocity dispersion and uncertainty consistent with the aforementioned central values.

As the broad shape of the χ^2 function displayed in the

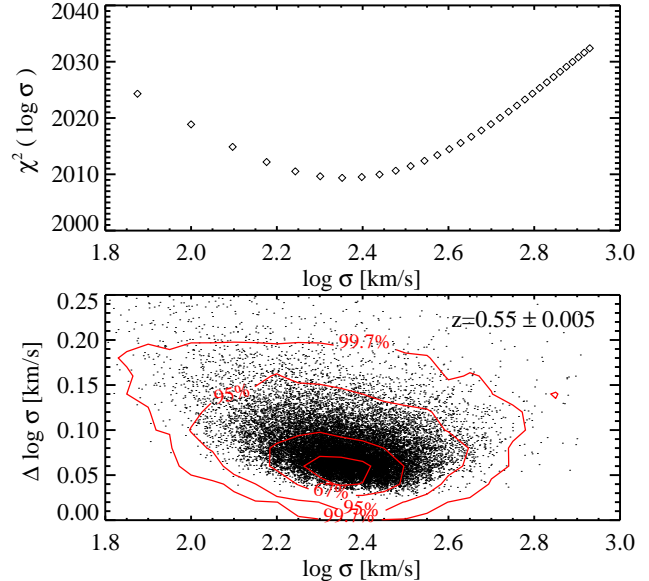


Figure 1. An illustration of the BOSS velocity dispersion data. *Top panel:* a typical $\chi^2(\sigma)$ curve as a function of the trial σ (D.O.F.=1736). This particular galaxy within the redshift range $z = 0.55 \pm 0.005$ is chosen to have best-fit velocity dispersion and uncertainty matching the densest region shown in the bottom panel plot. *Bottom panel:* scatter plot of the best-fit velocity dispersion in logarithmic scale and its uncertainty (also in logarithmic scale, black dots) for red CMASS galaxies ($g - i > 2.35$) within the redshift range $z = 0.55 \pm 0.005$. Contours that enclose 30%, 67%, 95%, and 99.7% of this subsample are overplotted in red.

top panel of Figure 1 indicates (and as also emphasized in Shu et al. 2012), a point estimate for the velocity dispersion is only partially informative, even after a dedicated treatment is adopted for the new χ^2 calculation. Note that an appreciable fraction of this subsample have best-fit velocity dispersions equal to 0 km/s due to the limitations of fitting low SN spectra. Using the likelihood function propagates all information to the higher level analysis of the entire population. That is one of the main motivations for employing a hierarchical Bayesian statistical approach in this paper.

4 BIMODALITY IN THE COLOUR-COLOUR PLANE: THE INTRINSIC RED SEQUENCE DISTRIBUTION

A key element in the computation of the intrinsic L - σ relation for the RS from the CMASS sample is the underlying intrinsic RS magnitude and colour distribution. This aspect is thoroughly addressed in MD2014, where we present an analytical method for deconvolving the observed (g-r) colour - (r-i) colour - (i)-band magnitude CMASS distributions

from the blurring effect produced by photometric errors and selection cuts. The CMASS sample comprises a considerable fraction of bluer objects, that can scatter into the red side of the colour-colour plane due to photometric errors. In MD2014, this aspect is treated by modeling the BC and the RS separately (red/blue deconvolution), which allows us to correct the RS intrinsic distribution from the contamination caused by BC objects. Importantly, this modeling is not performed from the basis of previous assumptions about “blue” or “red” objects based on stellar population synthesis models, but is intended to describe the bimodality found in the colour-colour plane. With this consideration, these components present the following characteristics:

- *Red Sequence (RS)*: The RS is so narrow that is consistent, within the errors, at fixed magnitude and for a narrow redshift slice, with a delta function in the colour-colour plane (width < 0.05 mag), with only a shallow colour-magnitude relation shifting the location of this point. The results reported in this paper regarding the L - σ relation are based on this intrinsic distribution.

- *Blue Cloud (BC)*: The BC is defined as a background distribution that contains *everything not belonging to the RS* and is well described by a more extended 2-D Gaussian in the colour-colour plane. The RS is superimposed upon the BC, that extends through the red side of the colour-colour plane. Again, the name “BC” is not meant to imply that this distribution contains only blue, young objects; the BC is a spectroscopically and photometrically heterogeneous population to which other types of ETGs can pertain, such as dusty ellipticals not belonging to the narrow RS.

The intrinsic distribution of magnitudes for the RS is the key ingredient in the computation of the RS L - σ relation, and this is provided in MD2014 in the form of the RS LF. For the sake of convenience, and given the very narrow redshift slices that we consider, we will constrain the $\log_{10} \sigma - m_i$ (apparent magnitude in the i band) relation (note that this is not the L - σ relation, which involves absolute magnitudes). As we show in the following section, for constraining this relation, it suffices to know the shape of the intrinsic distribution of apparent magnitudes, which is given by a Schechter Function of the form:

$$n_{sch}(m_i, \phi_*, m_*, \alpha) = 0.4 \log(10) \phi_* \left[10^{0.4(m_* - m_i)(\alpha + 1)} \right] \times \exp\left(-10^{0.4(m_* - m_i)}\right) \quad (2)$$

where $\alpha = -1$ and $\phi_* = \text{unity}$, for the sake of simplicity. The assumption that $\alpha = -1$ is dictated by the narrow magnitude range, that prohibits fitting for α . The intrinsic RS i -band magnitude distribution, as a function of redshift, can be obtained by inserting the following linear relation for the redshift evolution of the characteristic magnitude m_* into Equation 2:

$$m_*^{RS}(z) = (4.425 \pm 0.125) (z - 0.55) + (20.370 \pm 0.007) \quad (3)$$

Similarly, for the BC:

$$m_*^{BC}(z) = (4.011 \pm 0.178) (z - 0.55) + (20.730 \pm 0.010) \quad (4)$$

All the relations provided in this section come from the analysis presented in MD2014, although they are not explicitly reported there. By using these linear relations instead of the best fit values at each redshift we avoid introducing unnecessary noise into the analysis. These relations are obtained within the redshift range $0.525 < z < 0.65$, where selection effects are less severe. Note that the BC LF was not reported in MD2014 due to the extreme incompleteness affecting the BC in the CMASS sample. Instead, it is used as a means of accounting for the contribution of the BC in the sample and of subtracting this contribution from the RS LF. Following the same strategy, we compute the $\log_{10} \sigma - m_i$ relation for the BC (and later the BC L - σ relation) only as a means of subtracting the contribution of the BC on the RS $\log_{10} \sigma - m_i$ relation.

The last ingredient in the computation of the RS $\log_{10} \sigma - m_i$ relation, as we show in the next section, is the fraction of BC objects in the CMASS sample, i.e., f_{blue} , which is also provided in MD2014. Again, to avoid introducing noise in the computation, we use the following linear relation for the redshift dependence of f_{blue} :

$$f_{blue}(z) = (0.890 \pm 0.051) (z - 0.55) + (0.381 \pm 0.003) \quad (5)$$

5 PDSO: FORMALISM FOR THE PHOTOMETRIC DECONVOLUTION OF SPECTROSCOPIC OBSERVABLES

5.1 The method

The L - σ relation is a relation between a spectroscopic observable, the stellar velocity dispersion σ , and a photometric observable, the luminosity L (or, in a more practical fashion, the $\log_{10} \sigma$ and the absolute magnitude M). As previously mentioned, measuring velocity dispersions from BOSS galaxies is hindered by low SN spectra, which dictates that instead of point measurements we use likelihood functions for the velocity dispersions. The photometric aspect of the L - σ relation computation presents challenges as well: as discussed in MD2014, the observed CMASS distribution is strongly affected by photometric errors and selection effects. In this section we present a formalism that combines our likelihood measurements for the velocity dispersions and our red/blue deconvolution of photometric quantities. This formalism, which we call PDSO, can be used for the photometric deconvolution of any spectroscopic observables, so we will present it in a general way.

Let us start by assuming that we have a sample of galaxies indexed by i , each of which has a spectroscopic data vector \mathbf{d}_i (in our case, velocity dispersions) and a photometric

data vector \mathbf{c}_i (colours and/or magnitudes). These galaxies are selected (i.e., for measuring the spectra) according to some photometric cuts described by $P(\mathbf{c})$, which is the probability (between 0 and 1) of selecting a galaxy with photometric data vector \mathbf{c} . $P(\mathbf{c})$ in the case of the BOSS CMASS sample can be straightforwardly derived from the CMASS selection scheme (see Dawson et al. 2013).

Assume that we have quantified the probabilistic mapping from *intrinsic* (noise-free) photometric values \mathbf{C} into observed (noisy) photometric values \mathbf{c} , which we denote as $p(\mathbf{c}|\mathbf{C})$. In MD2014 this mapping is obtained by modeling the covariance matrix of magnitudes and colours using SDSS Stripe 82 multi-epoch data.

Assume that these galaxies have been quantified in terms of a number of one or more photometrically distinct population components indexed by k , with the results expressed as the intrinsic number density of galaxies per unit \mathbf{C} in component k , denoted by $n_k(\mathbf{C})$ such that $n_k(\mathbf{C}) d\mathbf{C}$ has units of spatial number density. In reality, as we will show below, this quantity can also have units of number. The above characterization can come in the form of the decomposition into RS and BC galaxy colour–luminosity functions. Note that $n_k(\mathbf{C})$ need not be normalized over \mathbf{C} , and indeed may be divergent.

As a result of the previous analysis, we have derived the individual probability density functions (PDF’s) of each component in observed space within the selected sample, as well as the fraction of sampled objects in each component. To express these in terms of previously introduced quantities, we introduce the following function for notational convenience:

$$\Phi_k(\mathbf{c}) = P(\mathbf{c}) \int d\mathbf{C} p(\mathbf{c}|\mathbf{C}) n_k(\mathbf{C}). \quad (6)$$

This is the number (density) of galaxies in observed photometric space for component k .

The number of galaxies in the sample in component k is

$$N_k = \int d\mathbf{c} \Phi_k(\mathbf{c}) \quad (7)$$

The fraction of sample galaxies pertaining to component k is

$$f_k = N_k / \sum_{k'} N_{k'}. \quad (8)$$

Note that f_k would correspond to f_{blue} (and $1 - f_{blue}$) within our deconvolution framework. The PDF of galaxies in observed photometric space in component k is

$$p_k(\mathbf{c}) = \Phi_k(\mathbf{c}) / N_k. \quad (9)$$

The full PDF of the observed sample in observed photometric space is

$$p(\mathbf{c}) = \sum_k f_k p_k(\mathbf{c}). \quad (10)$$

A derived function that we will make use of below is the

PDF of a sample galaxy in *intrinsic* photometric space given its position in *observed* photometric space, which we can derive by noting that the joint PDF of observed and intrinsic photometric vectors for component k is proportional as

$$p_k(\mathbf{C}, \mathbf{c}) \propto P(\mathbf{c}) p(\mathbf{c}|\mathbf{C}) n_k(\mathbf{C}) \quad (11)$$

so that then

$$p_k(\mathbf{C}|\mathbf{c}) = \frac{p_k(\mathbf{C}, \mathbf{c})}{\int d\mathbf{C} p_k(\mathbf{C}, \mathbf{c})} \quad (12)$$

$$= \frac{P(\mathbf{c}) p(\mathbf{c}|\mathbf{C}) n_k(\mathbf{C})}{\int d\mathbf{C} P(\mathbf{c}) p(\mathbf{c}|\mathbf{C}) n_k(\mathbf{C})} \quad (13)$$

$$= \frac{p(\mathbf{c}|\mathbf{C}) n_k(\mathbf{C})}{\int d\mathbf{C} p(\mathbf{c}|\mathbf{C}) n_k(\mathbf{C})} \quad (14)$$

Importantly, $p_k(\mathbf{C}|\mathbf{c})$, which is the function that we will use ultimately, is independent of some of the choices that we make about the intrinsic distributions, $n_k(\mathbf{C})$. In particular, any normalization will cancel off, so we can simply use the intrinsic number counts shown in Equation 2, where volume is not taken into account and $\phi_* = 1$ unity by definition.

Now assume that there is some parameter or vector of parameters \mathbf{x} that can be measured from the spectroscopic data vector \mathbf{d}_i in the sense that we can write down and compute the function

$$p(\mathbf{d}_i|\mathbf{x}_i) \quad (15)$$

for each galaxy i . In our case, \mathbf{x} is the velocity dispersion, σ and $p(\mathbf{d}_i|\mathbf{x}_i)$ is proportional to the function $\exp[-\chi^2(\sigma)]$.

Next we assume a parameterized model for the variation of the spectroscopic observable within the sample populations as a function of photometric values. This is expressed as

$$p_k(\mathbf{x}|\mathbf{C}; \mathbf{t}). \quad (16)$$

The vector \mathbf{t} will denote the “hyperparameters” that describe this PDF. Our goal is to infer the elements of \mathbf{t} . To do this, we proceed to express the likelihood function of \mathbf{t} given the spectroscopic data and the photometric data. In our framework, the hyperparameters \mathbf{t} only affect the probabilities of the spectroscopic observables *given* the photometric observations.

$$\mathcal{L}(\mathbf{t}|\{\mathbf{d}_i\}, \{\mathbf{c}_i\}) = p(\{\mathbf{d}_i\}|\{\mathbf{c}_i\}, \mathbf{t}) \quad (17)$$

$$= \prod_i p(\mathbf{d}_i|\mathbf{c}_i, \mathbf{t}) \quad (18)$$

$$= \prod_i \int d\mathbf{x} p(\mathbf{d}_i|\mathbf{x}) p(\mathbf{x}|\mathbf{c}_i, \mathbf{t}) \quad (19)$$

$$= \prod_i \int d\mathbf{x} p(\mathbf{d}_i|\mathbf{x}) \sum_k f_k p_k(\mathbf{x}|\mathbf{c}_i, \mathbf{t}) \quad (20)$$

$$= \prod_i \int d\mathbf{x} p(\mathbf{d}_i|\mathbf{x}) \sum_k f_k \int d\mathbf{C} p_k(\mathbf{x}|\mathbf{C}, \mathbf{t}) p_k(\mathbf{C}|\mathbf{c}_i) \quad (21)$$

At this point, we have arrived at an expression on the right-hand side entirely in terms of quantities that we have introduced above, and we can proceed to map and/or maximize the likelihood function of the hyperparameters \mathbf{t} .

5.2 Application to the computation of the L- σ relation in BOSS

For the sake of convenience, we proceed by applying our formalism to the computation of the $\log_{10} \sigma - m_i$ relation from the CMASS sample. Our spectroscopic observable is therefore the logarithm of the velocity dispersion, i.e. $\log_{10} \sigma$, and the intrinsic distributions (n_k) are represented by the Schechter number counts of Equation 2, with a redshift dependence given by Equations 3 and 4 for the RS and the BC, respectively. This choice implies that \mathbf{C} and \mathbf{c} correspond to the i-band apparent magnitude, m_i , in intrinsic and observed space, respectively.

The parameterized model for the variation of the spectroscopic observable ($\log_{10} \sigma$) within the sample populations as a function of photometric values (m_i) encodes the $\log_{10} \sigma - m_i$ relation. Motivated by results from Bernardi et al. (2003a), we approximate the intrinsic distribution of velocity dispersions at fixed L as a Gaussian distribution in $\log_{10} \sigma$ with mean $\langle \log_{10} \sigma \rangle$ and intrinsic scatter s . For component k this has the form:

$$p_k(\log_{10} \sigma | \mathbf{m}_i; \mathbf{t}_k) = \frac{1}{\sqrt{2\pi}s_k} \exp \left[\frac{-(\log_{10} \sigma - \langle \log_{10} \sigma \rangle_k)^2}{2s_k^2} \right] \quad (22)$$

The mean of the velocity dispersion for component k, i.e., $\langle \log_{10} \sigma \rangle_k$, is assumed to follow a linear relation with apparent magnitude, m_i , of the form:

$$\langle \log_{10} \sigma \rangle_k = c_{1,k} + 2.5 + c_{2,k}(m_i - 19) \quad (23)$$

This expression, as we will show in following sections, can be easily transformed, within our framework, into the L- σ relation, which is expressed in terms of absolute magnitudes.

6 APERTURE CORRECTION

BOSS velocity dispersions are measured within the 2 arcsec diameter aperture of the BOSS fibers. As we move to higher redshift within the CMASS sample, the angular size of the fiber probes progressively larger physical scales. This effect is accounted for *a posteriori*, by applying an aperture correction (AC) to the best-fit relations obtained by maximizing the likelihood function of Equation 21. By assuming a de Vaucouleurs profile for the variation of the surface brightness as a function of apparent distance to the center of the galaxy, we have obtained the following relation:

$$\sigma_{obs}/\sigma(\langle R_e \rangle) = 0.98 (R_e/R_{aperture})^{0.048} \quad (24)$$

that relates the observed velocity dispersion σ_{obs} that we measure in BOSS, the velocity dispersion averaged within the effective radius, R_e , and the effective radius itself, in arcsec. As part of the derivation of the above relation, the

blurring produced by an average seeing of 1.8 arcsec has been assumed.

In order to perform a realistic AC we need to take into account the variation of R_e as a function of apparent magnitude, m_i , for each redshift slice, which may affect the slope of the $\log_{10} \sigma - m_i$ relation. To this end, we fit a linear relation to the mean observed i-band $\log_{10} R_e$ measured by the pipeline (in arcsec) as a function of m_i ¹. For a given redshift slice, this relation takes the form:

$$\langle \log_{10} R_e \rangle = a + b(m_i - 19) \quad (25)$$

where we have shifted the reference magnitude to $m_i = 19$, similarly to Equation 23, for consistency. Figure 2 displays the observed i-band $\log_{10} R_e$ in arcsec as a function of m_i for the redshift slice centered at $z = 0.55$, in contours enclosing 67%, 95% and 99.7% of the entire sample, respectively. The squares show the mean values in magnitude bins of 0.1 mag and the errors the 1- σ scatter around the mean. The solid line shows the linear fit to the mean values that we use to correct, on average, our $\log_{10} \sigma - m_i$ relation.

By using Equation 24, it can be easily demonstrated that the aperture-corrected c_1 parameter, i.e. c_1^{ac} , is related to parameter a in Equation 25 in the following way:

$$c_1^{ac} = c_1 - 0.048a - \log_{10}(0.98) \quad (26)$$

And, similarly, for c_2^{ac} :

$$c_2^{ac} = c_2 - 0.048b \quad (27)$$

Within the same redshift slice, more luminous galaxies are larger in size (see Figure 2), which implies $b < 0$. The AC correction by definition tends, therefore, to steepen the L- σ relation.

In order to avoid introducing any extra noise we use a linear fit to the values of a and b as a function redshift, $a(z)$, $b(z)$. This is shown in Figure 3 for the redshift range of interest, $0.5 < z < 0.7$. The linear fit that we obtain for $a(z)$ is:

$$a(z) = (1.47 \pm 0.16)z + (-0.61 \pm 0.09) \quad (28)$$

and for $b(z)$:

$$b(z) = (-0.57 \pm 0.32)z + (-0.08 \pm 0.19) \quad (29)$$

Note that the error on the slope of $b(z)$ is large, so we will consider also the case where $b(z)$ is constant and equal to the mean value within the redshift range $0.52 < z < 0.65$, i.e. $b(z) = -0.402 \pm 0.020$.

¹ Beifiori et al. 2014 present an analysis on the evolution of the effective radius in BOSS, but the R_e - magnitude relation necessary to derive the aperture correction is not reported.

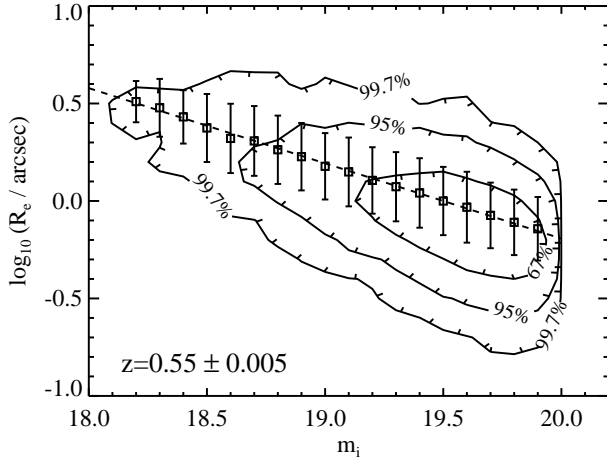


Figure 2. The observed i-band $\log_{10} R_e$ in arcsec as a function of the i-band apparent magnitude m_i for the redshift slice centered at $z = 0.55$, in contours enclosing 67%, 95% and 99.7% of the entire subsample, respectively. The squares show the mean values in magnitude bins of 0.1 mag and the errors the $1\text{-}\sigma$ scatter around the mean. The solid line shows a linear fit to the mean values.

A typical value of $b(z) = -0.402$ implies a correction on the slope of the $\log_{10} \sigma$ - m_i relation (the c_2 parameter) of ~ 0.02 . Within our framework, the slope of the $\log_{10} \sigma$ - m_i relation at a given redshift slice coincides with the slope of the L - σ relation. As a reference, typical values for this slope are ~ -0.1 (or equivalently 4 for the exponent β in the form $L \propto \sigma^\beta$; this is the F-J relation). This implies that the AC has a significant effect on the slope of the L - σ relation when computed from BOSS. The main idea is that brighter (and hence larger) galaxies have their velocity dispersions corrected by a different factor than fainter (and hence smaller) galaxies, for a given fixed angular aperture, which affects the slope of the L - σ relation.

It is interesting to compare the effect of adopting a different aperture correction on the $\log_{10} \sigma$ - m_i relation. Equations 26 and 27, in combination with the values of parameters $a(z)$ and $b(z)$, dictate the sensitivity of the AC to the exponent in Equation 24. By varying this exponent between a reasonable range, we can evaluate the effect on the zero-point and slope of the $\log_{10} \sigma$ - m_i relation. We have chosen a range between 0.04 (corresponding to the value derived by Jorgensen et al. 1995) and 0.066 (found by Cappellari et al. 2006). The majority of values adopted in the literature are within this range (e.g. Mehlert et al. 2003 estimate a value of 0.06).

Using Equations 26, and given that the typical variation of $a(z)$ within the redshift range considered is ~ 0.2 (see Figure 3), we find that the variation in the AC for the zero-point, ΔAC , within the redshift range considered (note that a is a function of redshift), for an exponent of 0.048, is 0.0096 dex, in absolute values. Increasing the exponent of

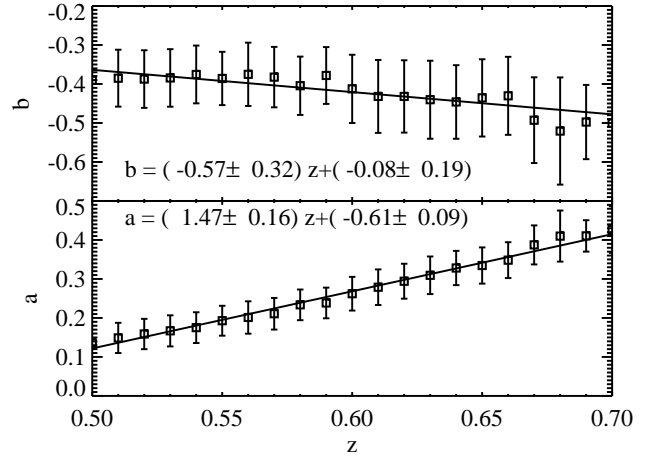


Figure 3. The redshift dependence of parameters b (upper panel, squares) and a (lower panel, squares), representing, respectively, the slope and the zero-point of the mean relation between the observed i-band $\log_{10} R_e$ (in arcsec) and the i-band apparent magnitude m_i . Errors correspond to uncertainty in the fit associated to each parameter. The solid lines show the linear fits that we use to correct our L - σ relation measurements.

the AC function to 0.066 would translate into an increase in ΔAC , for the zero-point, of a 38%. On the other hand, decreasing the exponent of the AC function to 0.04 would result in a ΔAC 17% smaller. Although the net effect is small, these variations can modify the zero-point - redshift trend. In Section 7.3 we discuss the redshift evolution of the zero-point, concluding that the effect on the zero-point of the uncertainties on the AC is significant, given the narrow redshift range that we probe and the mild evolution that we measure for the zero-point.

With regard to the slope, from Equation 27 and Figure 3, as mentioned above, we find that the typical AC on this parameter is ~ 0.02 (i.e. $b(z) \times 0.048$), basically independent of redshift. Adopting a range of values for the exponent of the AC correction 0.04 - 0.066 would translate into corrections within the range 0.016 - 0.026. Although the effect is not negligible, adopting a different AC would not modify the main conclusion of the paper, in terms of the steep slope of the L - σ relation, in any qualitative way (see following sections).

7 RESULTS

7.1 Best-fit parameters for the $\log_{10} \sigma$ - m_i relation

By maximizing the likelihood function of Equation 21, we obtain the best-fit values for the hyperparameters \mathbf{t} . These parameters are the following, for each component k (RS and BC): $c_{1,k}$, the zero-point of the $\log_{10} \sigma$ - m_i relation, that corresponds to the mean $\log_{10} \sigma$ at $m_i = 19$; $c_{2,k}$, the slope of

this linear relation, and s_k , the intrinsic scatter. The optimization of the likelihood function has been performed from $z = 0.40$ to $z = 0.70$, using a bin size of $\Delta z = 0.01$. This redshift range exceeds the redshift interval where the computation of the RS LF is more reliable, i.e. $0.52 \lesssim z \lesssim 0.65$. Results outside this high-confidence range are obtained by extrapolation of the linear fits to the redshift evolution of the intrinsic distribution and the fraction of blue objects in the sample.

Figure 4 displays the redshift evolution of the 3 best-fit hyperparameters \mathbf{t} , for both the RS and the BC. It is important to bear in mind that, due to extreme incompleteness, our BC component is not representative of the entire BC population, so we simply use it as a means of correcting for the contribution of BC objects in the sample. In each panel, this BC component is represented in blue lines/symbols. The aperture-corrected RS parameters are represented in red and the uncorrected RS parameters, in green.

Statistical errors on each parameter are obtained by mapping the likelihood function within the 6-dimension hyperspace and computing the posterior probability distribution for each parameter. This computation yields very small errors, which is consistent with the rapid convergence of the algorithm. While this procedure might not take all the possible sources of error into account, other more realistic options, such as a bootstrap analysis, are computationally challenging. In order to avoid underestimating our uncertainties, we take a conservative approach here and, instead of the aforementioned error, we use, as the real error, the scatter on each parameter (standard deviation) with respect to the best-fit relation with redshift.

In the upper panel of Figure 4, the $2.5 + c_{1,RS}$ increases linearly with redshift, from a value of ~ 2.43 at $z = 0.50$ to ~ 2.53 at $z = 0.70$. The aperture correction has very little effect on the zero-point of the $\log_{10} \sigma - m_i$ relation. The following linear relation is obtained for the aperture-corrected RS c_1 (hereafter we drop the *ac* superindex for simplicity):

$$2.5 + c_{1,RS}(z) = (2.235 \pm 0.009) + (0.381 \pm 0.016) z \quad (30)$$

At fixed apparent magnitude ($m_i = 19$), we look at progressively more luminous galaxies as we move to higher redshift. The $L - \sigma$ relation implies that more luminous RS galaxies have higher velocity dispersions, which explains the $c_{1,RS}$ - redshift trend. On the other hand, the BC represents a photometrically and spectroscopically heterogeneous population that contains a large fraction of blue, spiral galaxies (or even disk ellipticals) for which we expect smaller velocity dispersions. At fixed absolute magnitude, the BC component is expected, therefore, to have smaller mean $\log_{10} \sigma$ than the RS, which is exactly what the upper panel of Figure 4 shows.

The middle panel of Figure 4 shows the redshift evolution of the slope of the $\log_{10} \sigma - m_i$ relation, c_2 . The RS is consistent with a single point in the colour-colour plane, with a shallow colour-magnitude relation that we neglect in the

computation of K-corrections. Absolute magnitudes are simply obtained by rescaling the apparent magnitudes at each redshift slice. This result implies that $c_{2,RS}$ coincides with the slope of the $L - \sigma$ relation, as we explicitly show in the next section. Our results for $c_{2,RS}$ indicate little evolution in the slope of the $\log_{10} \sigma - m_i$ within the redshift range considered. Importantly, the AC, as discussed previously, has a significant effect on $c_{2,RS}$, i.e., that changes from ~ -0.07 to ~ -0.05 . The following linear relation with redshift is obtained for the aperture corrected $c_{2,RS}$:

$$c_{2,RS}(z) = -(0.033 \pm 0.012) - (0.029 \pm 0.021) z \quad (31)$$

As mentioned above, this dependence of $c_{2,RS}$ with redshift is not significant given the scatter in the data. The $\Delta\chi^2$ with respect to the redshift-independent assumption is only 1.57 (i.e. a significance of 1.25σ). The slope in the $\log_{10} \sigma - m_i$ relation that we measure within the redshift range $0.5 < z < 0.7$ is therefore -0.070 ± 0.006 before AC and -0.050 ± 0.007 after. The middle panel of Figure 4 also shows in a black dashed line our results for $c_{2,RS}$ assuming a constant value for the AC parameter b of $b(z) = -0.042$. Neglecting the redshift evolution of b in Figure 3 has little impact on $c_{2,RS}$.

The bottom panel of Figure 4 displays the redshift evolution of the intrinsic scatter in the $\log_{10} \sigma - m_i$ relation for both the RS and the BC component. This is the intrinsic RMS scatter in $\log_{10} \sigma$, at fixed m_i . Note that an ‘‘orthogonal’’ version of our result (i.e., scatter perpendicular to the $\log_{10} \sigma - m_i$ relation) would be essentially the same, given the steep slope that we measure for this relation. The scatter for the RS, s_{RS} , increases slightly with redshift, but this trend is not significant given the computed errors (the $\Delta\chi^2$ with respect to the redshift-independent assumption is only 1.36, i.e., a significance of 1.17σ). The mean value that we obtain is only $s_{RS} = 0.047 \pm 0.004$ in $\log_{10} \sigma$. This value for the scatter in the $\log_{10} \sigma - m_i$ relation is very small as compared to the typical value of ~ 0.1 found at intermediate-mass ranges and low redshift. In Section 8 we show his this result is in excellent agreement with previous low- z high-mass results.

The hyperparameter s for the BC component is significantly larger, i.e., ~ 0.12 . Keep in mind that the BC component in our sample is by no means complete, and therefore, the corresponding s value that we measure does not represent the true scatter for the entire BC population. It does provide, however, some indication of the scatter of the BC population relative to the RS population. The value of ~ 0.12 is consistent with the intrinsic scatter trends shown by Shu et al. (2012), who without accounting for the contamination effect caused by the BC objects, find that the overall intrinsic scatter value for the CMASS galaxy sample is ~ 0.1 , an intermediate value due to the mixture of both RS and BC galaxies. A trend of higher intrinsic scatter at higher redshift is also discovered by Shu et al. (2012), which

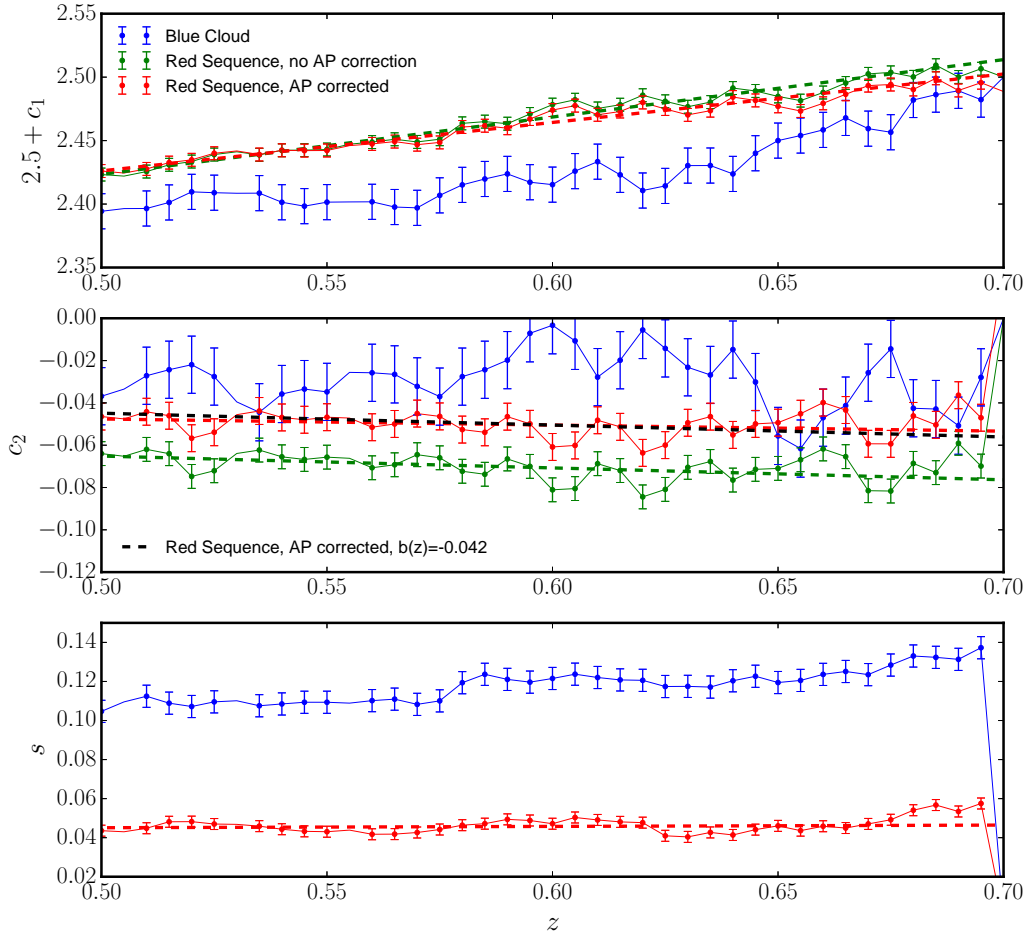


Figure 4. The best-fit values for the hyperparameters \mathbf{t} that describe the $\log_{10} \sigma$ - m_i relation for both the RS and the BC component as a function of redshift. The distribution of velocity dispersions, for each component, is approximated as a log-normal distribution in $\log_{10} \sigma$ with mean $\langle \log_{10} \sigma \rangle$ and intrinsic scatter s . The mean is parametrized as $\langle \log_{10} \sigma \rangle = c_1 + 2.5 + c_2 (m_i - 19)$. In each panel, dots and solid lines represent the best-fit values obtained by maximizing the likelihood function of Equation 21, following our hierarchical Bayesian analysis. Blue lines/symbols represent the $\log_{10} \sigma$ - m_i relation for the BC component, red lines/symbols show this relation for the RS component, once aperture correction is performed, and green lines/symbols show our results before aperture correction. Dashed lines show the best-fit linear models obtained within the redshift range considered. The black dashed line in the second panel represents a linear fit where aperture correction to c_2 is assumed to be independent of redshift and equal to $b(z) = -0.042$. Errors on the best-fit parameters are assumed to be equal to the standard deviation with respect to the best-fit model in each parameter.

can be explained by the fact that the relative fraction of the BC objects in the CMASS sample increases with redshift.

The $\log_{10} \sigma$ - m_i relation in a magnitude- $\log_{10} \sigma$ diagram for 4 different redshift slices is explicitly shown in Figure 5 (Method 1, see next section).

7.2 The effect of the various corrections implemented

Our computation of the $\log_{10} \sigma - m_i$ (equivalent to the L - σ relation) at $z \sim 0.55$ incorporates accurate treatments of various issues affecting the BOSS data. In particular, we cor-

rect for incompleteness within the colour-colour-magnitude space, and we separately model the intrinsic RS and BC populations, which allows the statistical removal of all BC in the CMASS sample, including those that are predicted to scatter through the red side of the colour-colour plane (see MD2014 for more details). This information is incorporated into our PDSO method, a hierarchical Bayesian statistical framework that allows us to utilize the stellar velocity dispersion likelihood functions of individual objects, instead of the point estimates associated to them. This section is intended to provide a sense as to what impact these corrections have on our $\log_{10} \sigma - m_i$ results.

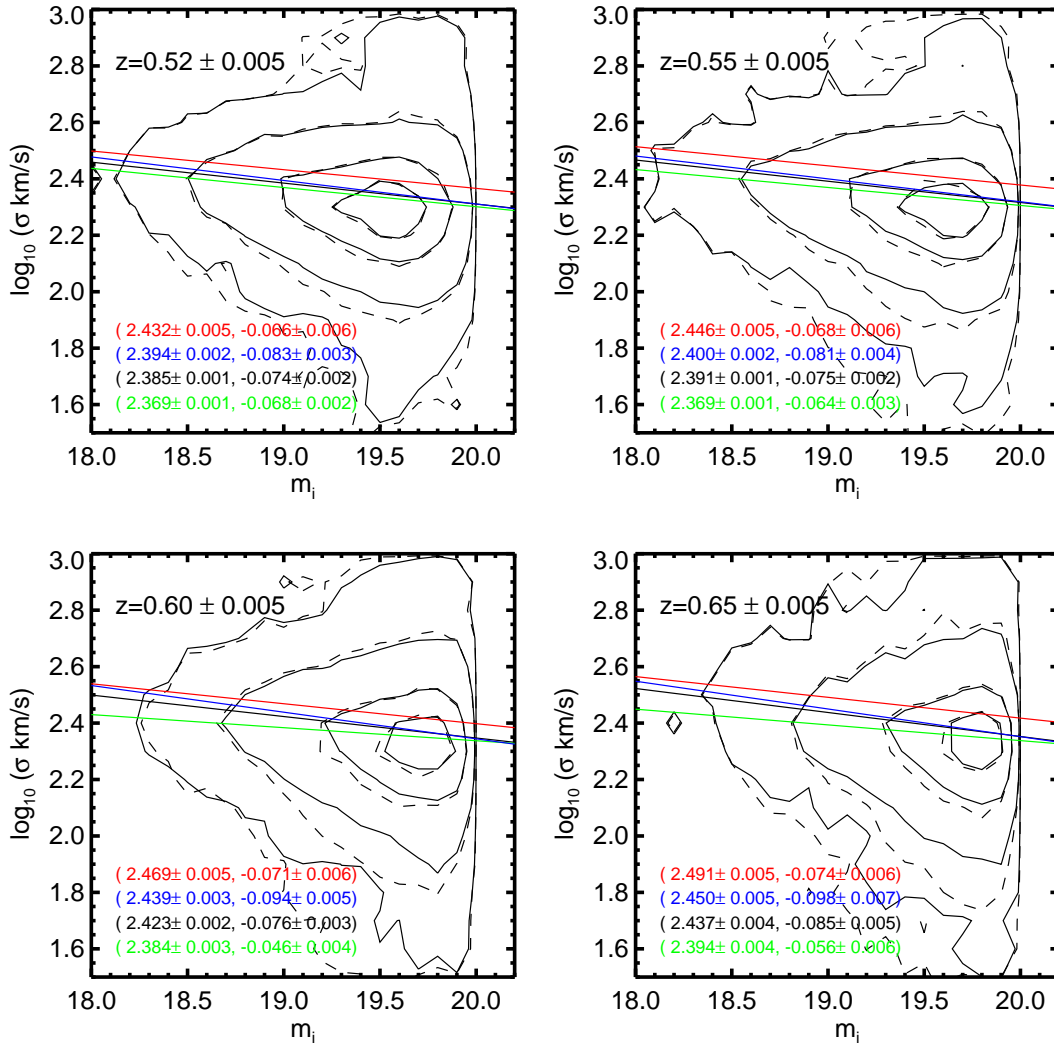


Figure 5. The $\log_{10} \sigma - m_i$ relation as obtained using 4 different methods in 4 different redshift slices ($z = 0.52, 0.55, 0.60, 0.65$). Results from Method 1, 2, 3, and 4 (see text) are shown in red, blue, black and green, respectively. The solid contours show the best-fit central velocity dispersions (point estimates) as a function of apparent magnitude once a colour cut $g - i > 2.35$ is applied to remove blue objects, and the dashed contours represent the entire sample. The best-fit values for the slope and zero-point of the $\log_{10} \sigma - m_i$ are also provided.

In order to illustrate the effect of each correction, we have computed the $\log_{10} \sigma - m_i$ relation using the following 4 methods:

- **Method 1:** This is our optimized method, including all the corrections mentioned above.
- **Method 2:** This uses exactly the same methodology as the one implemented in Shu et al. (2012), applied to the

dataset used in this work. Shu et al. (2012) developed of a hierarchical approach that incorporates velocity dispersion likelihood functions. The main differences with Method 1 are that 1) the whole CMASS sample is used for the computation, without any red-blue deconvolution, and 2) only a very approximative completeness correction is applied. For

the sake of comparison, here we exclude blue objects by imposing a simple colour cut $g - i > 2.35$ in observed space.

- **Method 3:** The observed L - σ relation for the blue sub-sample defined using a simple colour cut $g - i > 2.35$. No red-blue deconvolution or completeness correction is applied. Instead of velocity dispersion likelihood functions, point estimates for the velocity dispersion are used.

- **Method 4:** Same as Method 3, but for the entire CMASS sample.

7.2.1 Effect on the slope and the zero-point

In Figure 5 and Figure 6 we compare in 4 different redshift slices ($z = 0.52, 0.55, 0.60, 0.65$) the $\log_{10} \sigma - m_i$ relation computed using the 4 methods presented above. Figure 5 displays these relations in a $\log_{10} \sigma$ vs. m_i diagram, where the solid contours show the best-fit central velocity dispersions (point estimates) as a function of apparent magnitude once the colour demarcation is applied, and the dashed contours represent the entire sample. Figure 6 shows the redshift trends for the zero-point and the slope (not aperture-corrected, for simplicity), respectively.

With regard to the zero-point, Figure 5 and especially the upper panel of Figure 6, indicate that an inadequate or partial removal of blue objects in the sample tends to artificially push this parameter towards smaller values. This is expected, given that the velocity dispersion is obviously smaller in bluer (typically spiral) galaxies (see also the upper panel of Figure 4). A partial removal of blue objects using a colour cut (Method 2) only palliates this effect slightly. We would still measure a zero point 10% smaller than that of the intrinsic RS distribution. Part of this difference can also be due to the fact that in Method 2 completeness is also only partially addressed, by just applying a rough correction to account for the scatter of objects in and out different magnitude bins, due to photometric errors. Interestingly, a comparison between the zero-point obtained from Method 2 and Method 3 shows that, for the same sample (both using a colour cut in observed space, no deconvolution), the use of velocity dispersion likelihood functions in the context of a hierarchical Bayesian approach (Method 2) has a minor effect on the measured zero-point.

The effect of corrections on the pre-aperture-corrected slope of the $\log_{10} \sigma - m_i$ relation is less obvious. The lower panel of Figure 6 shows that the measured slope obtained with the optimized Method 1 is only slightly steeper (larger in this figure) than what we would measure using the observed distribution alone (with a colour cut, i.e., Method 3). This differences would likely be within the errors once the slope is aperture corrected (see following section). Interestingly, using Shu et al. (2012) method, i.e. Method 2, would lead to a pre-aperture-corrected slope much closer to the canonical value of 4 (i.e. -0.1 in this figure), 15 – 25% shallower than the values obtained with Method 1 (note that we would still measure a slope steeper than the canonical value once aperture correction is applied).

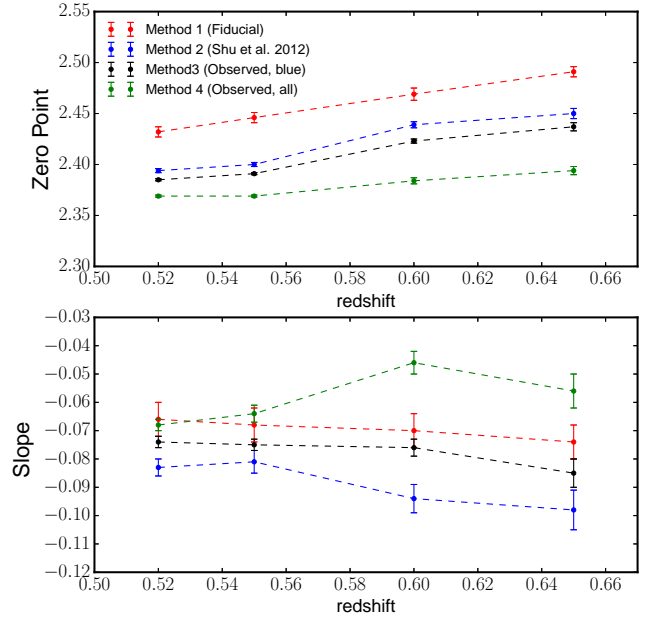


Figure 6. Zero-point (upper panel) and slope (lower panel) as a function of redshift obtained using the 4 different methods explained in the text (results from Method 1, 2, 3, and 4 are shown in red, blue, black and green, respectively).

7.2.2 Effect on the scatter

The use of velocity dispersion likelihood functions in combination with completeness/intrinsic distribution results within a hierarchical Bayesian statistical framework has a tremendous impact on our ability to recover the intrinsic scatter in the $\log_{10} \sigma - m_i$ relation (which coincides with the scatter in the L - σ relation). The typical observed scatter in Figure 5 ranges from ~ 0.1 at the bright end to ~ 0.16 at the faint end. For the entire, partially-completeness-corrected observed distribution, Shu et al. (2012) report a value of ~ 0.1 , which is in agreement with the scatter in the higher-SN regime (within the sample). Our comprehensive analysis allows us to dig even deeper, unveiling the intrinsic scatter of the intrinsic RS distribution: a tiny 0.05 dex, as Figure 4 shows.

The difference between the scatter that we measure and the one reported by Shu et al. (2012) illustrates the importance of the red-blue deconvolution. As shown in the bottom panel of Figure 4, the scatter that we expect for the BC population is significantly larger. This is consistent with the fact that the BC is a much more extended distribution (photometrically and spectroscopically heterogenous) in the colour-colour plane. Mixing RS and BC objects and not properly correcting for completeness inevitably leads to an increase in the reported intrinsic scatter of the L - σ relation.

In order to demonstrate that we actually have the statistical power to measure such a small scatter, we have per-

formed a simple Monte Carlo variance-estimation analysis to estimate the resolution that we can expect given the number of objects that we have in a typical redshift bin ($\sim 20,000$ objects) and the typical error that we have in our individual velocity dispersion measurements (~ 0.1 dex, as Figure 1 shows). By simulating the observed distribution of velocity dispersions assuming an intrinsic scatter of 0.047 dex in $\log_{10} \sigma$ and the aforementioned typical measurement error on $\log_{10} \sigma$, we can evaluate our capacity to recover the intrinsic scatter. Our analysis shows that the typical uncertainty on the intrinsic scatter is of the order of 0.001 dex, which is more than one order of magnitude smaller than the value that we find for the scatter, i.e. 0.047 dex in $\log_{10} \sigma$. Note that the error that we estimate for the scatter is 0.004 dex. This test gives us confidence that our measurement is not an artifact that results from working below our resolution limit.

7.3 The L- σ relation

Translating the best-fit hyperparameters shown in Figure 4 into the standard L- σ relation ($\log_{10} \sigma$ as a function of absolute magnitude) for the RS is straightforward, due to the intrinsic characteristics of the RS colour-colour-magnitude distribution. In MD2014 we show that, at a given narrow redshift slice (width $\Delta z = 0.01$), and magnitude bin, the RS intrinsic distribution is consistent with a single point in the colour-colour plane, with only a shallow colour-magnitude relation that shifts this point slightly with L. Under such conditions, the K-correction, independently of the stellar population synthesis model chosen, changes very little within the apparent magnitude range of the CMASS sample, so we can basically assume it to be constant. We can, therefore, convert from apparent magnitudes to absolute magnitudes (K-corrected to $z = 0.55$) at a given redshift slice by simply rescaling the apparent magnitude using the standard equation:

$${}^{0.55}M_i = m_i - DM(z) - {}^{0.55}K_i(z) \quad (32)$$

The width of each redshift slice is small enough that the variation of DM within the redshift bin can also be neglected. By substituting Equation 32 into Equation 23, rearranging and adding a factor $M_0 c_2$ at each side of the equation we arrive at the following expression:

$$\langle \log_{10} \sigma \rangle = c'_1 + 2.5 + c'_2 ({}^{0.55}M_i - M_0) \quad (33)$$

where:

$$\begin{aligned} c'_1(z) &= c_1(z) - c_2(z)(19 - DM(z) - {}^{0.55}K_i(z) - M_0) \\ c'_2(z) &= c_2(z) \end{aligned} \quad (34)$$

The slope of the L- σ relation is independent of the fact that we use apparent magnitudes or absolute magnitudes, again due to the characteristic shape of the RS in

colour-colour-magnitude space. The K-correction as a function of redshift, ${}^{0.55}K_i(z)$, is computed using a grid of models generated using the Flexible Stellar Population Synthesis code (FSPS, Conroy et al. 2009) in the way described in MD2014. This grid expands a range of plausible stellar population properties for redshift-dependent models within the CMASS redshift range. An average K-correction assuming the colours of the RS is computed at every redshift.

Figure 7 displays parameters c'_1 and c'_2 for the L- σ relation as a function of redshift, assuming ${}^{0.55}M_0 = -23$ (black). Errors are assumed to be equal to the standard deviation of the data for each parameter. The value of ${}^{0.55}M_0 = -23$ for the reference absolute magnitude has been chosen because it falls within the CMASS magnitude range across the entire redshift range considered (see MD2014).

As Figure 7 indicates, the zero-point that we measure for the L- σ relation has a slight dependence on redshift, so that larger values are found at higher redshifts. It is, however, a very small effect, of ~ 0.005 dex within the redshift range considered ($0.5 < z < 0.7$, ~ 1.3 Gyr of cosmic time). The best-fit linear relation that we measure is $2.429 \pm 0.007 + (0.023 \pm 0.011) z$ (black dashed line). This redshift dependence is significant as compared to a best-fit redshift-independent value of $c'_1 = 2.443 \pm 0.004$ if we consider the whole redshift range ($\Delta\chi^2 = 4.49$, i.e., a significance of $\sim 2\sigma$), but not if we restrict ourselves to the high-confidence redshift range $0.52 < z < 0.65$ ($\Delta\chi^2 = 1.579$, i.e., a significance of $\sim 1.25\sigma$).

In MD2014 we conclude that the LF evolution of the LRG population at $z \sim 0.55$ is consistent with that of a passively-evolving population that fades at a rate of 1.18 mag per unit redshift. Assuming plausible single-stellar population models, including both Flexible Stellar Population Synthesis (FSPS, Conroy et al. 2009) and M09 (Maraston et al. 2009) models, such fading rate, at that redshift, translates into a formation redshift for the LRGs of $z = 2-3$. The evolution of the zero-point assuming a best-fit passive model of the aforementioned characteristics is shown in a red dashed line in Figure 7. Here, by best-fit model we mean that the normalization of the zero-point of the passive model is fit to the data points, so only the redshift evolution is meaningful. The deviations found between our fiducial model (the best-fit model that we obtained from our photometric deconvolution formalism) and the best-fit passive model are of the order of ± 0.004 dex within the entire redshift range $0.5 < z < 0.7$. These deviations are again significant ($\Delta\chi^2 = 10.24$, i.e., a significance of $\sim 3.2\sigma$) if we considered the entire redshift range, but that significance is questionable if we restrict ourselves to the high-confidence redshift range ($\Delta\chi^2 = 3.01$, i.e., a significance of $\sim 1.73\sigma$).

The fact that the significance of the discrepancies with the best-fit passive model reported in MD2014 depend strongly on the redshift range considered, in combination with the fact the effect is so small (± 0.004 dex), appear to suggest that our results for the zero-point - redshift trend are consistent with the best-fit passive model. This idea is

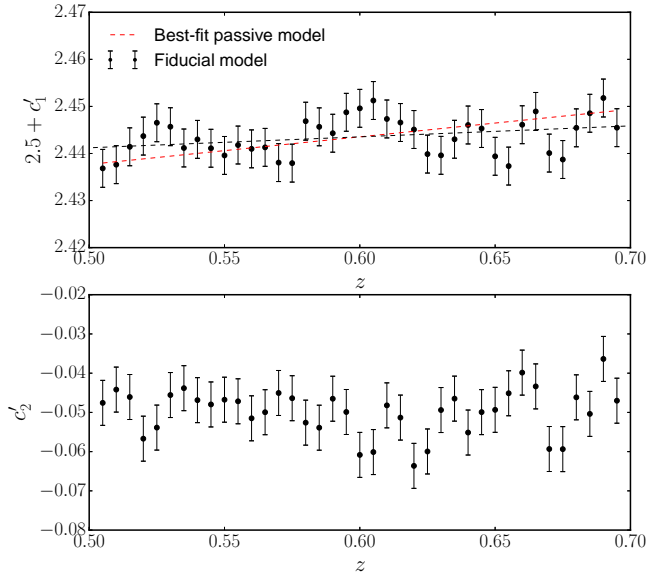


Figure 7. The aperture-corrected L - σ relation parameters as a function of redshift within the redshift range $0.5 < z < 0.7$. Upper panel: The zero-point or, equivalently, the mean of the $\log_{10} \sigma$ at a K -corrected reference magnitude of $^{0.55}M_i = -23$ (black dots), and the best-fit linear model its redshift evolution (black dashed line). In addition, we show the best-fit passive model that fades at a rate of 1.18 mag per unit redshift (as measured in MD2014). Lower panel: the slope of the L - σ relation, c'_2 . Errors are assumed to be equal to the standard deviation with respect to the best-fit model for each parameter.

reinforced when we consider the uncertainty on the computation of the AC. A modification of the AC, within reasonable limits, would produce an effect of the same magnitude as the discrepancies that we find between the data and the best-fit passive model. As a matter of fact, a variation of the $a(z)$ and $b(z)$ functions involved in the AC, within the reported uncertainties, could account for the discrepancies found. More importantly, the trend shown in Figure 7 is sensitive to the exponent of the AC, as discussed in Section 6. We have checked that by increasing slightly this exponent we can rapidly reach a much better agreement between the model and the data. A value of 0.06 (instead of 0.048), which is within the typical range of values previously used in literature, would produce almost a perfect agreement (a tiny $\Delta\chi^2 = 0.11$, when using the entire redshift range).

In summary, we conclude that our results are consistent with a passive model with formation redshift $z = 2 - 3$, given the small variation of the zero-point that we measure within such a narrow redshift range and the uncertainties that the AC is subject to. This result is in good agreement with a variety of studies on the evolution of the FP, as we discuss in Section 8.1. An improvement in the AC or R_e estimation in BOSS will be necessary to further constrain the evolution of the zero-point. The possibility remains that

the discrepancies found may also be partially due to the fading rate of the passive model being too high; a value closer to ~ 0.9 mag per unit redshift would suffice to make these discrepancies clearly not significant. This, in any case, would not imply a formation redshift much higher than $z = 2 - 3$, given the typical fading-rate evolution of passive models (see MD2014 for a discussion).

8 DISCUSSION

8.1 Comparison with previous results

In this section we show that our results for the high-mass L - σ relation at $z \sim 0.55$ are in good agreement with previous findings at low redshift.

The canonical form of the L - σ relation for our chosen bandpass is $L_i \propto \sigma^\beta$, where L_i represents the i -band luminosity. The slope of this relation, β , is directly related to the measured slope of the $\log_{10} \sigma$ - M_i relation, m'_2 , as

$$\beta = -\frac{0.4}{c'_2}. \quad (35)$$

As we have shown, the mean value of c'_2 for the RS, within the high-confidence redshift range, is -0.070 ± 0.006 , before AC is applied. This value implies a L - σ relation slope of $\beta = 5.71 \pm 0.49$. Imposing a constant offset of -0.019 to the slope, as introduced by the AC according to Equation 27, the aperture-corrected L - σ relation becomes even steeper, with a mean slope of $\beta = 7.83 \pm 1.11$.

The above measurement has been performed with a sample of more than 600,000 massive LRGs, with a mean stellar mass of $M_* \simeq 10^{11.3} M_\odot$, within the redshift range $0.5 < z < 0.7$. At intermediate mass ranges and $z \sim 0.1$, using ETG samples extracted from the SDSS, it has been shown that the slope of the L - σ relation is consistent with that of a canonical F-J relation, i.e. ~ 4 (Bernardi et al. 2003a; Desroches et al. 2007). Even though this is a fairly robust result, studies at these mass ranges might still be subject to an inadequate treatment of selection effects. As an example, La Barbera et al. (2010), using the SDSS-UKIDSS survey, report a slope of ~ 5 for a sample at a similar mass range.

At higher mass ranges, the curvature of the L - σ relation has also been detected at high statistical significance at $z \sim 0.1$ using the SDSS (Desroches et al. 2007, Hyde & Bernardi 2009a, Bernardi et al. 2011). However, a definite quantification of the high-mass slope has not emerged. Desroches et al. (2007) report a slope of ~ 4.5 at $M_r \geq -24$ (or $\log_{10} \sigma \gtrsim 2.4$). The authors find a much steeper slope, of ~ 5.9 , for a subsample of brightest cluster galaxies (BCGs).

Some other works have focused on small samples of ETGs in the nearby universe (of dozens to a couple of hundred objects). While these samples are strongly affected by low-number statistics, they have the advantage that galaxy properties can be measured with higher precision.

Lauer et al. (2007a), using a compilation of HST observations of a sample of 219 ETGs, measure a slope for the L- σ relation of ~ 7 for a subsample of core and BCG ellipticals, the latter being predominantly core ellipticals as well (note that Bernardi et al. 2007, using an SDSS sample, report a significantly steeper slope for BCGs as compare to normal ETGs; from their Figure 6 we can visually estimate a slope of ~ 8). Core ellipticals are identified by the fact that the central light profile is a shallow power law separated by a break from the outer, steep Sersic function profile. A value of ~ 2 is reported for the coreless or "power-law" elliptical subsample, a class of objects that present steep cusps in surface brightness. Interestingly, a number of studies suggest that core ellipticals dominate at the high-mass end, whereas coreless ellipticals are predominant at lower masses (see e.g. Faber et al. 2007; Lauer et al. 2007b,a; Hyde et al. 2008). Subsequently, Kormendy & Bender (2013), using a similar sample with some corrections and slight modifications in the core/coreless classification, estimate a slope of ~ 8 for the core sample alone, and close to the canonical value of 4 for the coreless sample. Our results for the slope of the L- σ relation are in excellent agreement with these studies, in terms of core ellipticals.

Results consistent with the above picture are also obtained from the ATLAS^{3D} sample (Cappellari et al. 2011), comprising 260 local-volume ETGs. Cappellari et al. (2013) measure a high-mass slope of ~ 4.7 (for the related stellar mass M- σ relation). This result is obtained above a characteristic stellar mass of $\sim 2 \times 10^{11} M_{\odot}$, a range of masses where the ETG population in this sample is again reportedly dominated by core ellipticals. Note that a detection of this mass scale in a *statistically-significant* sample came with the SDSS (Bernardi et al. 2011). This scale corresponds approximately to the range of masses covered by BOSS.

Independently of the central brightness profile classification, a steep slope at the bright/massive end is confirmed by other studies. In the environment analysis of Focardi & Malavasi (2012) (using a small sample of a few hundred objects extracted from HYPERLEDA, Paturel et al. 2003) a value of ~ 5.6 is reported at high luminosities, although the authors indicate that an alternative method to compute this slope could yield a value closer to 4.5.

To summarize, we have drawn two main conclusions in terms of the slope of the high-mass L- σ relation from a study of previous literature at low redshift. Firstly, enough evidence has been gathered of a steeper slope at the high-mass end from SDSS works at $z \sim 0.1$. Secondly, the reported value for the slope varies among different works, from ~ 4.5 to ~ 8 . Note that the L- σ relation is sensitive to low-number / selection effects (which nearby samples are affected by), but also to the region of the FP probed (in particular, to the exact luminosity range under analysis). Our work, provides, for the first time, a measurement at an unprecedented statistical significance of the slope at an intermediate redshift and at the highest-mass end, where the L- σ relation "saturates"

(using the terminology of Kormendy & Bender 2013, among other authors).

Another important result from this work is the small intrinsic scatter of the L- σ relation at the high-mass end at $z \sim 0.55$; a measurement that has been performed with high statistical significance for the first time. The scatter, quantified by the hyperparameter s in this work, is found to have a mean value of $s = 0.047 \pm 0.004$ in $\log_{10} \sigma$ at fixed L and redshift slice (with no significant redshift dependence). Again, in order to place these results in the context of previous literature we can only compare with nearby/low-redshift samples, where some clear indications have been reported that the intrinsic scatter is smaller at higher masses.

Figure 9 (right panel) from Hyde & Bernardi (2009a) clearly shows that the scatter in the L- σ relation (in particular, in the $\log_{10} \sigma - M_r$ relation) decreases towards high luminosities. In particular, we can visually estimate a value of ~ 0.05 dex at $M_r < -23$. A similar value for the scatter of the mass- σ relation at the high-mass end can be visually estimated from Figure 1 of Bernardi et al. (2011). Although these values are not explicitly reported, they are obtained from relatively large SDSS samples (the Bernardi et al. 2011 sample contains $\sim 18,000$ massive ETGs), which indicates that these results are statistically significant.

In nearby samples, however, low number statistics prevent a reliable estimation of the scatter. In any case, indications have been reported that the intrinsic scatter is smaller in core ellipticals, which would be consistent with our measurement. At the high-mass end, Kormendy & Bender (2013), by adopting measurement errors of 0.1 mag in magnitude and 0.03 in $\log_{10} \sigma$, report an intrinsic physical scatter of 0.06 in $\log_{10} \sigma$ for core galaxies and 0.10 in $\log_{10} \sigma$ for core-less galaxies at a given magnitude.

Even though we must be careful to compare results at the high-mass end from a quantitative point of view, a mass (or luminosity) dependence of the intrinsic scatter of the L- σ relation have been reported in other works, including Sheth et al. (2003), Desroches et al. (2007), Nigoche-Netro et al. (2011) and Focardi & Malavasi (2012).

Finally, our result that the evolution of the zero-point of the L- σ relation is consistent with a passive model with a formation redshift of $z = 2 - 3$ is in good agreement with the redshift evolution of the FP as measured in galaxy clusters up to $z \sim 1$ (see e.g. van Dokkum & Franx 1996 at $z = 0.39$; Kelson et al. 1997 at $z = 0.58$; van Dokkum et al. 1998 at $z = 0.83$; van Dokkum et al. 1998 at $z = 0.83$; Wuyts et al. 2004 at $z = 0.583$ and $z = 0.83$; van Dokkum & Stanford 2003; Holden et al. 2005 at $z \sim 1.25$). More generally, the result that the high-mass RS population evolves passively from a high formation redshift is in agreement with a wide array of analyses (see, e.g., Wake et al. 2006; Cool et al. 2008, MD2014 for LF results; Maraston et al. 2013 for LRG-SED evolution results; Guo et al. 2013, 2014 for LRG-clustering results).

In light of the above comparison, it appears that the

high-mass end of the L - σ relation not only remains unchanged within the redshift range $0.5 < z < 0.7$, but would also be consistent with $z \sim 0$ results.

8.2 Physical interpretation

The very steep slope of the L - σ relation at the high-mass end implies that the interplay between the different processes involved in shaping the evolution of RS galaxies at different mass ranges is systematically different. As galaxies grow, central velocity dispersions do not change as much as expected according to the scaling relations at lower masses. This result is consistent with the systematic variation of the total mass profile as a function of mass in the central region of ETGs found by Shu et al. (2015), so that more massive galaxies have shallower profiles. One possibility to explain this behavior is that the relative efficiencies of gas cooling and feedback in RS galaxies vary at different mass scales. Gas cooling permits baryons to condense in the central regions of galaxies, and therefore it is believed to make the mass distribution more centrally concentrated (e.g. Gnedin et al. 2004; Gustafsson et al. 2006; Abadi et al. 2010; Velliscig et al. 2014). Heating due to dynamical friction and supernovae (SN)/Active Galactic Nucleus (AGN) feedback, in contrast, can soften the central density concentration (e.g. Nipoti et al. 2004; Romano-Díaz et al. 2008; Governato et al. 2010; Duffy et al. 2010; Martizzi et al. 2012; Dubois et al. 2013; Velliscig et al. 2014). If feedback became more efficient in more massive galaxies, that could explain both the results presented here and in Shu et al. (2015).

A more straightforward explanation comes from a scenario where massive and intermediate-mass ETGs have a different evolutionary history. From high-resolution images of a small number of local ETGs, some evidence has been gathered that the high-mass end of the RS population might be occupied almost exclusively by core ellipticals, whereas coreless ellipticals dominate at intermediate and lower masses (Lauer et al. 2007b,a; Hyde et al. 2008; Cappellari et al. 2013). This transition occurs at $\log_{10} M_* \sim 11.2$, a mass scale that was first detected *with high-statistical significance by Bernardi et al. (2011)*. Even though this classification arises from the shape of the central surface brightness profile, several studies have shown that this bimodality, known as the “E-E dichotomy”, extends to a number of other galaxy properties: core ellipticals have boxy isophotes and are slow rotators while coreless ellipticals have more disk-like isophotes and rotate faster (to name but a few properties, see e.g. Kormendy & Bender 1996; Faber et al. 1997; Lauer et al. 2007b,a; Hyde et al. 2008; Cappellari et al. 2013; Kormendy & Bender 2013 for a complete discussion). Importantly, the above mass scale has been associated, with high statistical significance, with the curvature of the scaling relations (see Hyde & Bernardi 2009a; Bernardi et al. 2011).

This characterization confirms the ideas of

Kormendy & Bender 1996, who proposed a revision of the Hubble Sequence for elliptical galaxies, where isophote shape is used as an implicit indicator of velocity anisotropy. The general consensus is that the properties of these two distinct populations are the consequence of two different evolutionary paths. Massive core ellipticals appear to be formed through major dissipationless mergers (Lauer et al. 2007b,a; Bernardi et al. 2011; Cappellari et al. 2013; Kormendy & Bender 2013), whereas the less-massive coreless ellipticals seem to have undergone a more complex evolution (Kormendy et al. 2009 review evidence that they are formed in wet mergers with starbursts).

This paper provides the most precise measurements of the L - σ relation at the highest mass range ever probed with statistical significance. Unfortunately, however, BOSS does not provide the type of data required to perform a central surface brightness profile analysis that can confirm that the sample is dominated by core ellipticals, as previous results suggest. A complete analysis of this type would answer the question as to whether core ellipticals are fully responsible for the steep slope. This option is claimed by Kormendy & Bender (2013) by showing that the slope of the L - σ relation is significantly steeper for core galaxies even in the luminosity region where core and coreless galaxies overlap (recall the statistical limitations of the study). Independently of this discussion, the shallow dependence of σ on galaxy mass (obtained from a L - σ relation very similar to what we obtained) is reported in Kormendy & Bender (2013) to be approximately similar to N-body predictions (Nipoti et al. 2003; Boylan-Kolchin et al. 2006; Hilz et al. 2012) for dissipationless major mergers.

Previous literature about the “E-E dichotomy” along with the similarities between our measurements and those reported by Lauer et al. (2007b) and Kormendy & Bender (2013) suggest that the intrinsic high-mass RS distribution characterized in MD2014 (the same distribution for which we compute the L - σ relation here) can be identified as a core-elliptical population. In MD2014, the intrinsic RS distribution is photometrically deconvolved from photometric errors and selection effects. The resulting distribution is so narrow in the colour-colour plane that is consistent with a delta function, at fixed magnitude and narrow redshift slice (with a shallow colour-magnitude dependence for its location). The second component of the intrinsic model, the BC, is a more extended distribution, well described by a Gaussian function in the colour-colour plane, upon which the RS is superimposed. Our BC is defined as a background distribution including everything not belonging to the very-pronounced RS (see MD2014 for details). This BC actually extends through the red side of the colour-colour plane. This characterization could reflect the “E-E dichotomy” on the red side of the colour-colour plane, with this intrinsic BC being composed by a large fraction of coreless ellipticals, for which more scatter on the colour-colour plane is to be expected. Follow-up work will be needed to confirm this picture.

The intrinsic scatter of the L - σ relation at $z = 0.55$ adds to the result reported in MD2014 that the intrinsic RS distribution is extremely concentrated in the colour-colour plane as well (at fixed magnitude and narrow redshift slice), which is an indication that there is little variability as far as the stellar populations are concerned within this population. The small scatter in these relations is consistent with the idea that this is an aged quiescent population that has seen little activity in a long time.

The above idea is reinforced by the fact that the high-mass L - σ relation at $z = 0.55$ appears to be very similar to that reported at $z = 0.1$. Also, the evolution of the zero-point within the redshift range $0.5 < z < 0.7$ is consistent with that of a passively-evolving population that formed at redshift of $z = 2 - 3$, in agreement with the LF-evolution results shown in MD2014 for the same population. The picture of the evolution of the high-mass end of the RS is, however, not completely clarified yet. Bernardi et al. (2015) have recently analyzed the high-mass luminosity and stellar mass function evolution from the CMASS to the SDSS, reporting a puzzling result. The evolution of this functions appears to be “impressively” passive, when K+E corrections computed from the Maraston et al. (2009) models are used. However, when matched in comoving number- or luminosity-density, the SDSS galaxies are less strongly clustered than CMASS galaxies, which is obviously inconsistent with a passive evolution scenario.

9 CONCLUSIONS AND FUTURE APPLICATIONS

We have measured the intrinsic L - σ relation for massive, luminous red galaxies within the redshift range $0.5 < z < 0.7$. We achieve unprecedented precision at the high-mass end ($M_* \gtrsim 10^{11} M_\odot$) on the measurement of the parameters of the L - σ relation by using a sample of 600,000 galaxies from the BOSS CMASS sample (SDSS-III). We have deconvolved the effects of photometric and spectroscopic uncertainties and red–blue galaxy confusion using a novel hierarchical Bayesian formalism that is generally applicable to any combination of photometric and spectroscopic observables. The main conclusions of our analysis can be summarized as follows:

- At $z \sim 0.55$, the passively-evolved L - σ relation at $M_* \gtrsim 10^{11} M_\odot$ appears to be consistent with that at $z = 0.1$.
- The slope of the $z = 0.55$ L - σ relation at the high-mass end is $\beta = 7.83 \pm 1.11$, corresponding to the canonical form $L_i \propto \sigma^\beta$. This value confirms, with the highest statistical significance ever achieved, the idea of a curved mass-dependent L - σ relation. Scaling relations for the most massive LRGs are systematically different than the relations defined at lower masses.
- The intrinsic scatter on the L - σ relation is $s = 0.047 \pm 0.004$ in $\log_{10} \sigma$ at fixed L . This value confirms, with the

highest statistical significance ever achieved, that the intrinsic scatter decreases as a function of mass.

- We detect no significant evolution in the slope and scatter of the L - σ relation within the redshift range considered. Under a single stellar population assumption, the redshift evolution of the zero-point is consistent within the errors with that of a passively-evolving galaxy population that formed at redshift $z = 2 - 3$. This is in agreement with the LF-evolution results reported in MD2014 for the same population.

- Our results, in combination with those reported in MD2014, provide an accurate description of the high-mass end of the red sequence population at $z \sim 0.55$, which is characterized in MD2014 as an extremely narrow population in the optical colour-colour plane.

- Our results for the L - σ relation, in the light of previous literature, suggest that our high-mass RS distribution might be identified with the “core-elliptical” galaxy population. In light of the ETG dichotomy, the second component identified in MD2014, a much more extended distribution upon which the RS is superimposed, would contain a significant fraction of “coreless” ellipticals towards the red side. The larger scatter in colour found for this population would be consistent with the evolutionary path that has been proposed for coreless ellipticals.

The above results lead us to consider followup work intended to investigate core–coreless elliptical demographics in BOSS. This project will require the use of high-resolution data.

The success of our algorithm for the photometric deconvolution of spectroscopic observables opens a field of future applications, as it can be used to constrain the intrinsic distribution of a variety of spectroscopically-derived quantities in BOSS. In the broader picture, the statistical techniques developed in this work and in MD2014 lay the foundations for galaxy-evolution studies using other current and future dark energy surveys, like eBOSS, which are subject to the same type of SN limitations and selection effects that we face in BOSS.

The extensive characterization of the high-mass RS presented in this work and in MD2014 will be used in combination with N-body numerical simulations to investigate the intrinsic clustering properties of this galaxy population, along with the intrinsic connection between these galaxies and the dark matter haloes that they inhabit. The connection between galaxies and haloes will be performed by applying the techniques of halo occupation distributions (HOD: e.g., Berlind & Weinberg 2002; Zehavi et al. 2005) and halo abundance matching (HAM: e.g., Vale & Ostriker 2004; Trujillo-Gomez et al. 2011). This is a novel approach as compared with the previous clustering/halo-galaxy-connection studies in BOSS, which have focused on the observed galaxy distribution and lacked a proper completeness correction.

Finally, the velocity-dispersion distributions implied by the L - σ relation that we have obtained in this work can be used in combination with the luminosity-function results

of MD2014 to determine the statistical strong gravitational lensing cross section of the CMASS sample. This cross section can in turn be used to predict and interpret the incidence of spectroscopically selected strong lenses within large redshift surveys (e.g., Bolton et al. 2008, Brownstein et al. 2012, Arneson et al. 2012, Bolton et al. 2012), and to derive constraints on cosmological parameters from the statistics of gravitationally lensed quasars (e.g., Kochanek 1996, Chae et al. 2002, Mitchell et al. 2005).

ACKNOWLEDGMENTS

This material is based upon work supported by the U.S. Department of Energy, Office of Science, Office of High Energy Physics, under Award Number de-sc0010331.

The support and resources from the Center for High Performance Computing at the University of Utah are gratefully acknowledged.

Funding for SDSS-III has been provided by the Alfred P. Sloan Foundation, the Participating Institutions, the National Science Foundation, and the U.S. Department of Energy Office of Science. The SDSS-III Web site is <http://www.sdss3.org/>.

SDSS-III is managed by the Astrophysical Research Consortium for the Participating Institutions of the SDSS-III Collaboration including the University of Arizona, the Brazilian Participation Group, Brookhaven National Laboratory, University of Cambridge, University of Florida, the French Participation Group, the German Participation Group, the Instituto de Astrofísica de Canarias, the Michigan State/Notre Dame/JINA Participation Group, Johns Hopkins University, Lawrence Berkeley National Laboratory, Max Planck Institute for Astrophysics, New Mexico State University, New York University, Ohio State University, Pennsylvania State University, University of Portsmouth, Princeton University, the Spanish Participation Group, University of Tokyo, The University of Utah, Vanderbilt University, University of Virginia, University of Washington, and Yale University.

REFERENCES

- Abadi M. G., Navarro J. F., Fardal M., Babul A., Steinmetz M., 2010, *MNRAS*, 407, 435
- Ahn C. P., Alexandroff R., Allende Prieto C., et al., 2012, *ApJS*, 203, 21
- Ahn C. P., Alexandroff R., Allende Prieto C., et al., 2014, *ApJS*, 211, 17
- Aihara H., Allende Prieto C., An D., et al., 2011, *ApJS*, 193, 29
- Alam S., Albareti F. D., Allende Prieto C., et al., 2015, *ApJS*, 219, 12
- Anderson L., Aubourg É., Bailey S., et al., 2014, *MNRAS*, 441, 24
- Arneson R. A., Brownstein J. R., Bolton A. S., 2012, *ApJ*, 753, 4
- Beifiori A., Thomas D., Maraston C., et al., 2014, *ApJ*, 789, 92
- Berlind A. A., Weinberg D. H., 2002, *ApJ*, 575, 587
- Bernardi M., Hyde J. B., Sheth R. K., Miller C. J., Nichol R. C., 2007, *AJ*, 133, 1741
- Bernardi M., Meert A., Sheth R. K., et al., 2015, *ArXiv e-prints:1510.07702*
- Bernardi M., Meert A., Vikram V., et al., 2014, *MNRAS*, 443, 874
- Bernardi M., Roche N., Shankar F., Sheth R. K., 2011, *MNRAS*, 412, L6
- Bernardi M., Sheth R. K., Annis J., et al., 2003a, *AJ*, 125, 1849
- Bernardi M., Sheth R. K., Annis J., et al., 2003b, *AJ*, 125, 1866
- Bolton A. S., Brownstein J. R., Kochanek C. S., et al., 2012, *ApJ*, 757, 82
- Bolton A. S., Burles S., Koopmans L. V. E., et al., 2008, *ApJ*, 682, 964
- Boylan-Kolchin M., Ma C.-P., Quataert E., 2006, *MNRAS*, 369, 1081
- Brownstein J. R., Bolton A. S., Schlegel D. J., et al., 2012, *ApJ*, 744, 41
- Cappellari M., Bacon R., Bureau M., et al., 2006, *MNRAS*, 366, 1126
- Cappellari M., Emsellem E., Krajnović D., et al., 2011, *MNRAS*, 413, 813
- Cappellari M., McDermid R. M., Alatalo K., et al., 2013, *MNRAS*, 432, 1862
- Chae K.-H., Biggs A. D., Blandford R. D., et al., 2002, *Physical Review Letters*, 89, 15, 151301
- Conroy C., Gunn J. E., White M., 2009, *ApJ*, 699, 486
- Cool R. J., Eisenstein D. J., Fan X., et al., 2008, *ApJ*, 682, 919
- Davies R. L., Efstathiou G., Fall S. M., Illingworth G., Schechter P. L., 1983, *ApJ*, 266, 41
- Dawson K. S., Schlegel D. J., Ahn C. P., et al., 2013, *AJ*, 145, 10
- de Rijcke S., Michielsen D., Dejonghe H., Zeilinger W. W., Hau G. K. T., 2005, *A&A*, 438, 491
- de Vaucouleurs G., 1982a, *Nature*, 299, 303
- de Vaucouleurs G., 1982b, *The Observatory*, 102, 178
- Denicoló G., Terlevich R., Terlevich E., Forbes D. A., Terlevich A., 2005, *MNRAS*, 358, 813
- Desroches L.-B., Quataert E., Ma C.-P., West A. A., 2007, *MNRAS*, 377, 402
- Djorgovski S., Davis M., 1987, *ApJ*, 313, 59
- Dressler A., Lynden-Bell D., Burstein D., et al., 1987, *ApJ*, 313, 42
- Dubois Y., Gavazzi R., Peirani S., Silk J., 2013, *MNRAS*, 433, 3297
- Duffy A. R., Schaye J., Kay S. T., Dalla Vecchia C., Battye R. A., Booth C. M., 2010, *MNRAS*, 405, 2161
- Eisenstein D. J., Weinberg D. H., Agol E., et al., 2011, *AJ*,

- 142, 72
 Faber S. M., Jackson R. E., 1976, *ApJ*, 204, 668
 Faber S. M., Tremaine S., Ajhar E. A., et al., 1997, *AJ*, 114, 1771
 Faber S. M., Willmer C. N. A., Wolf C., et al., 2007, *ApJ*, 665, 265
 Focardi P., Malavasi N., 2012, *ApJ*, 756, 117
 Fritz A., Böhm A., Ziegler B. L., 2009, *MNRAS*, 393, 1467
 Fukugita M., Ichikawa T., Gunn J. E., Doi M., Shimasaku K., Schneider D. P., 1996, *AJ*, 111, 1748
 Gnedin O. Y., Kravtsov A. V., Klypin A. A., Nagai D., 2004, *ApJ*, 616, 16
 Governato F., Brook C., Mayer L., et al., 2010, *Nature*, 463, 203
 Gunn J. E., Carr M., Rockosi C., et al., 1998, *AJ*, 116, 3040
 Gunn J. E., Siegmund W. A., Mannery E. J., et al., 2006, *AJ*, 131, 2332
 Guo H., Zehavi I., Zheng Z., et al., 2013, *ApJ*, 767, 122
 Guo H., Zheng Z., Zehavi I., et al., 2014, *MNRAS*, 441, 2398
 Gustafsson M., Fairbairn M., Sommer-Larsen J., 2006, *PhRvD*, 74, 12, 123522
 Held E. V., de Zeeuw T., Mould J., Picard A., 1992, *AJ*, 103, 851
 Hilz M., Naab T., Ostriker J. P., Thomas J., Burkert A., Jesseit R., 2012, *MNRAS*, 425, 3119
 Holden B. P., Blakeslee J. P., Postman M., et al., 2005, *ApJ*, 626, 809
 Hyde J. B., Bernardi M., 2009a, *MNRAS*, 394, 1978
 Hyde J. B., Bernardi M., 2009b, *MNRAS*, 396, 1171
 Hyde J. B., Bernardi M., Sheth R. K., Nichol R. C., 2008, *MNRAS*, 391, 1559
 Jørgensen I., Chiboucas K., Flint K., Bergmann M., Barr J., Davies R., 2006, *ApJL*, 639, L9
 Jørgensen I., Franx M., Kjaergaard P., 1995, *MNRAS*, 276, 1341
 Kelson D. D., van Dokkum P. G., Franx M., Illingworth G. D., Fabricant D., 1997, *ApJL*, 478, L13
 Kochanek C. S., 1996, *ApJ*, 466, 638
 Komatsu E., Smith K. M., Dunkley J., et al., 2011, *ApJS*, 192, 18
 Kormendy J., Bender R., 1996, *ApJL*, 464, L119
 Kormendy J., Bender R., 2013, *ApJL*, 769, L5
 Kormendy J., Fisher D. B., Cornell M. E., Bender R., 2009, *ApJS*, 182, 216
 Kroupa P., 2001, *MNRAS*, 322, 231
 La Barbera F., de Carvalho R. R., de La Rosa I. G., Lopes P. A. A., 2010, *MNRAS*, 408, 1335
 Lauer T. R., Faber S. M., Richstone D., et al., 2007a, *ApJ*, 662, 808
 Lauer T. R., Gebhardt K., Faber S. M., et al., 2007b, *ApJ*, 664, 226
 Magoulas C., Springob C. M., Colless M., et al., 2012, *MNRAS*, 427, 245
 Malumuth E. M., Kirshner R. P., 1981, *ApJ*, 251, 508
 Maraston C., Pforr J., Henriques B. M., et al., 2013, *MNRAS*, 435, 2764
 Maraston C., Strömbäck G., Thomas D., Wake D. A., Nichol R. C., 2009, *MNRAS*, 394, L107
 Martizzi D., Teyssier R., Moore B., Wentz T., 2012, *MNRAS*, 422, 3081
 Masters K. L., Maraston C., Nichol R. C., et al., 2011, *MNRAS*, 418, 1055
 Matkovic A., Guzmán R., 2007, in *Revista Mexicana de Astronomía y Astrofísica Conference Series*, edited by R. Guzmán, vol. 29 of *Revista Mexicana de Astronomía y Astrofísica*, vol. 27, 107–109
 Mehlert D., Thomas D., Saglia R. P., Bender R., Wegner G., 2003, *A&A*, 407, 423
 Minkowski R., 1962, in *Problems of Extra-Galactic Research*, edited by G. C. McVittie, vol. 15 of *IAU Symposium*, 112
 Mitchell J. L., Keeton C. R., Frieman J. A., Sheth R. K., 2005, *ApJ*, 622, 81
 Montero-Dorta A. D., Bolton A. S., Brownstein J. R., et al., 2014, *ArXiv e-prints*, arXiv:1410.5854
 Morton D. C., Chevalier R. A., 1973, *ApJ*, 179, 55
 Nigoche-Netro A., Aguerri J. A. L., Lagos P., et al., 2011, *A&A*, 534, A61
 Nigoche-Netro A., Aguerri J. A. L., Lagos P., Ruelas-Mayorga A., Sánchez L. J., Machado A., 2010, *A&A*, 516, A96
 Nipoti C., Londrillo P., Ciotti L., 2003, *MNRAS*, 342, 501
 Nipoti C., Treu T., Ciotti L., Stiavelli M., 2004, *MNRAS*, 355, 1119
 Oke J. B., Gunn J. E., 1983, *ApJ*, 266, 713
 Oser L., Naab T., Ostriker J. P., Johansson P. H., 2012, *ApJ*, 744, 63
 Pahre M. A., de Carvalho R. R., Djorgovski S. G., 1998, *AJ*, 116, 1606
 Paturel G., Garnier R., 1992, *A&A*, 254, 93
 Paturel G., Petit C., Prugniel P., et al., 2003, *A&A*, 412, 45
 Porter L. A., Somerville R. S., Primack J. R., Johansson P. H., 2014, *MNRAS*, 444, 942
 Posti L., Nipoti C., Stiavelli M., Ciotti L., 2014, *MNRAS*, 440, 610
 Reda F. M., Forbes D. A., Beasley M. A., O’Sullivan E. J., Goudfrooij P., 2004, *MNRAS*, 354, 851
 Reda F. M., Forbes D. A., Hau G. K. T., 2005, *MNRAS*, 360, 693
 Reid B., Ho S., Padmanabhan N., et al., 2015, *ArXiv e-prints*: 1509.06529
 Romano-Díaz E., Shlosman I., Hoffman Y., Heller C., 2008, *ApJL*, 685, L105
 Schechter P. L., 1980, *AJ*, 85, 801
 Shankar F., Marulli F., Bernardi M., Mei S., Meert A., Vikram V., 2013, *MNRAS*, 428, 109
 Sheth R. K., Bernardi M., Schechter P. L., et al., 2003, *ApJ*, 594, 225
 Shu Y., Bolton A. S., Brownstein J. R., et al., 2015, *ApJ*, 803, 71

- Shu Y., Bolton A. S., Schlegel D. J., et al., 2012, *AJ*, 143, 90
- Smee S. A., Gunn J. E., Uomoto A., et al., 2013, *AJ*, 146, 32
- Tonry J. L., 1981, *ApJL*, 251, L1
- Treu T., Stiavelli M., Bertin G., Casertano S., Møller P., 2001, *MNRAS*, 326, 237
- Trujillo-Gomez S., Klypin A., Primack J., Romanowsky A. J., 2011, *ApJ*, 742, 16
- Vale A., Ostriker J. P., 2004, *MNRAS*, 353, 189
- van Dokkum P. G., Franx M., 1996, *MNRAS*, 281, 985
- van Dokkum P. G., Franx M., Kelson D. D., Illingworth G. D., 1998, *ApJL*, 504, L17
- van Dokkum P. G., Stanford S. A., 2003, *ApJ*, 585, 78
- Velliscig M., van Daalen M. P., Schaye J., et al., 2014, *MNRAS*, 442, 2641
- von der Linden A., Best P. N., Kauffmann G., White S. D. M., 2007, *MNRAS*, 379, 867
- Wake D. A., Nichol R. C., Eisenstein D. J., et al., 2006, *MNRAS*, 372, 537
- Wuyts S., van Dokkum P. G., Kelson D. D., Franx M., Illingworth G. D., 2004, *ApJ*, 605, 677
- York D. G., Adelman J., Anderson Jr. J. E., et al., 2000, *AJ*, 120, 1579
- Zehavi I., Zheng Z., Weinberg D. H., et al., 2005, *ApJ*, 630, 1